

Application Examples

In this chapter, examples for the identification of processes from different areas are presented. These examples cover processes as diverse as electric and fluidic actuators, robots and machine tools, internal combustion engines and automotive vehicles up to heat exchangers and illustrate the application of the different methods. However, only a rough overview over the application of the various methods can be given. One will see that optimal results depend on various aspects. These include

- Design of the experiment and here especially the choice of the input signal and the signal conditioning (e.g. low-pass filtering)
- A priori knowledge about the process for the choice of the resulting model type
- Intended application of the derived model

It will become clear in the examples that different combinations of identification methods and filters will be required for different processes, as there will for example be models that have been identified in the time domain and others that have been identified in the frequency domain. Furthermore, there are usually static non-linear models as well as linear dynamic and non-linear dynamic models. Especially with regard to the final application, either continuous-time or discrete-time models are preferred. It will also be shown that the selected model structure and the selected identification method must depend on the physically given properties. Hence, physical (theoretical) modeling of the process is always a good starting point to gather a priori knowledge.

An overview of the examples to be presented in this chapter is found in Table 24.1. For each application example, the special symbols, that are used, are summarized under the corresponding model equations.

24.1 Actuators

This overview shall begin with electric and fluidic actuators, which are found widespread as actuators in automation systems in general and in mechatronic systems in particular. For a detailed treatment of all aspects ranging from construction

Table 24.1. Overview of examples covered in this chapter

Process (section in parentheses)	Continuous Time	Discrete Time	Time Domain	Frequency Domain	Linear	Non-Linear	Time-Variant	MIMO	Physical Model	Neural Net
Brushless DC Actuators (24.1.1)	✓		✓			✓			✓	
Normal DC motor for electric throttle (24.1.2)	✓		✓			✓			✓	
Hydraulic actuators (24.1.3)	✓		✓			✓			✓	
Machine tool (24.2.1)	✓		✓		✓				✓	
Industrial robot (24.2.2)	✓		✓			✓			✓	
Centrifugal pumps (24.2.3)	✓		✓			✓			✓	
Heat exchangers (24.2.4)	✓		✓		✓	✓	✓		(✓)	✓
Air conditioning (24.2.5)		✓	✓		✓					
Dehumidifier (24.2.6)		✓	✓		✓					
Engine teststand (24.2.7)	✓			✓	✓					
Estimation of vehicle parameters (24.3.1)	✓		✓		✓		✓	✓	✓	
Braking systems (24.3.2)	✓		✓			✓	✓		✓	
Automotive suspension (24.3.3)	✓		✓		✓	(✓)	✓		✓	
Tire pressure (24.3.4)			✓	✓	✓		✓			
Internal combustion engines (24.3.5)		✓	✓			✓		✓		✓

and design features to the specific advantages and disadvantages of individual realizations up to modeling and control, the reader is referred to the book by Isermann (2005) and with regards to applications for fault detection and diagnosis principles to (Isermann, 2010) and given references.

24.1.1 Brushless DC Actuators

As a first example for an electrically actuated system, the cabin outflow valve of a passenger aircraft is presented. The pressure in the fuselage of passenger aircraft flying above 2 000 m is permanently controlled. Fresh bleed air from the engines is constantly released at the front of the fuselage. At the fuselage tail, so-called cabin outflow valves are mounted, which allow the air from the cabin to escape to the surroundings. The valves are driven by brushless DC motors (BLDC) as illustrated in Fig. 24.1 (Moseler et al, 1999). For safety reasons, there is redundancy in the drive and there are two brushless DC motors, which act on a common gear. Another classical DC motor serves as an additional backup.

In the following, a dynamic model of the brushless DC motor and the driven load shall be set up and subsequently, the parameters shall be identified. The technical data of the motor have been summarized in Table 24.2.

As electric motors require a rotating magnetic field to keep up the movement of the rotor, traditional DC motors are equipped with a so-called *commutator*, which is

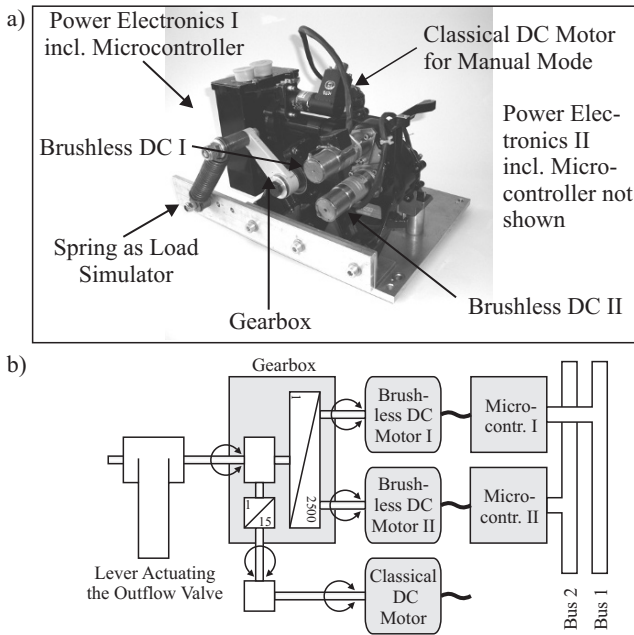


Fig. 24.1. Photo (a) and block diagram (b) of the cabin outflow valve

Table 24.2. Specifications of the BLDC motor

Parameter	Value
Weight	335 g
Length	87 mm
Diameter	30.5 mm
Supply voltage	28 V
Armature resistance	2.3 Ω
No-load speed	7 400 rpm
No-load current	50 mA
Short-circuit torque	28 mNm
Short-circuit current	1 A (Limited)

a mechanical device that changes the current feed of the rotor windings. A brushless DC motor uses an electronic circuit for this task. Here, the rotor is typically made up of a permanent magnet and the stator windings are supplied with current to generate an appropriately rotating magnetic field. As the rotor consists of permanent magnets only, no electric connection to the rotor is necessary. The position of the rotor is sensed by Hall sensors and is fed back to an electronic circuit that carries out the commutation, see Fig. 24.2. The advantage of the electronic commutation

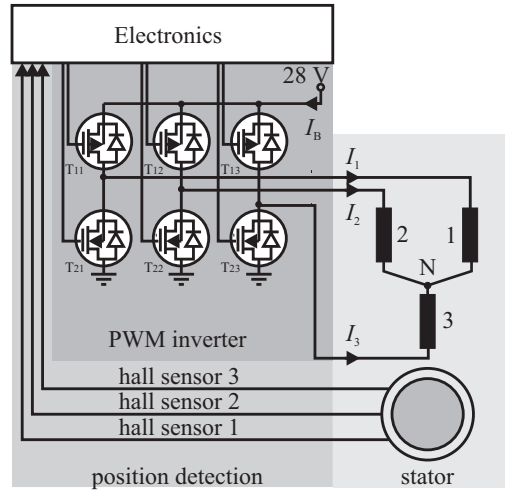


Fig. 24.2. Scheme of a brushless DC motor with electronic commutation realized by an integrated circuit and transistors

is that no brushes exist, which would be subject to wear-and-tear and could cause electromagnetic disturbances. Therefore, the reliability is relatively high.

The stator possesses 3 coils which are Y-connected and are driven by a PWM (pulse width modulation) inverter. The rotor has 4 permanent magnets. The position of the rotor magnets is measured by 3 Hall sensors mounted on the stator. These determine the switching sequence of 6 MOSFET transistors of the PWM inverter. This switching scheme is implemented in a separated programmable logic array. The PWM inverter is supplied with a fixed voltage U_B by the DC power supply and generates square wave voltages through the commutation logic via the 6 transistors to the 3 coils (phases).

Usually, only measurements of the supply voltage U_B , the input current I_B of the 6 phase full bridge circuit, and the angular rotor speed ω_R are available. However, for the detailed modeling that will be carried out in the following, also measurements of the phase current I_A and phase voltage U_A have been utilized. As the brushless DC motor switches the current over from one phase to the next as the rotor moves, the phase voltage and current refer to the *active* pair of phases (in star connection) that correlates with the rotor orientation.

The behavior of the motor can be described by the two differential equations

$$U_A(t) = R_A I_A(t) + L_A \frac{d}{dt} I_A(t) + \Psi \omega_R(t) \quad (24.1.1)$$

$$\Psi I_A(t) = J \frac{d}{dt} \omega_R(t) + M_V \omega_R(t) + M_C \text{sign } \omega_R(t) + M_L^* . \quad (24.1.2)$$

The electric and magneto-mechanic subsystem are coupled by the back emf as $U_{\text{emf}}(t) = \Psi \omega_R(t)$ and the electric torque $M_{\text{el}}(t) = \Psi I(t)$. The mechanic load

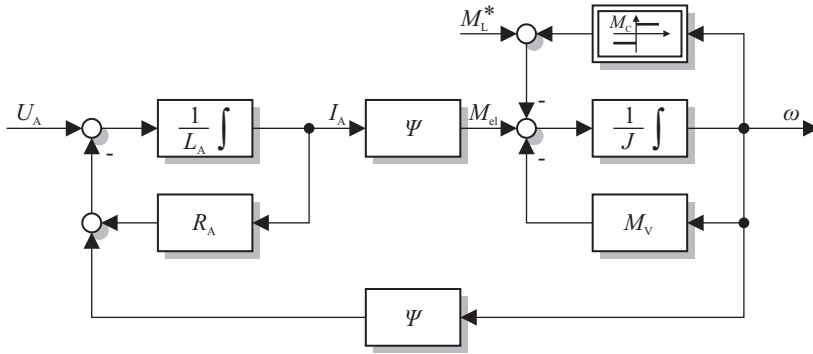


Fig. 24.3. Block diagram of the brushless DC motor model

is modeled as an inertia with both Coulomb and viscous friction. Also, an external load torque M_L is provided for. The drive shaft of the motor is coupled to the flap by means of a gear. The gear ratio ν relates the motor shaft position φ_R to the flap position φ_G

$$\varphi_G = \frac{\varphi_R}{\nu} \quad (24.1.3)$$

with $\nu = 2\,500$. The load torque of the flap is a normal function of the position φ_G

$$M_L = c_s f(\varphi_G) \quad (24.1.4)$$

and the kind of this characteristic is approximately known around the steady-state operation point. (For the experiments, the flap was replaced by a lever with a spring). All quantities have been transferred to the “motor” side, the referred load torque has been denoted as M_L^* . A block diagram is shown in Fig. 24.3. In this context, the following symbols are used:

L_A	armature inductance	J	inertia
R_A	armature resistance	M_C	coefficient of Coulomb friction
Ψ	torque constant	M_V	coefficient of viscous friction
ν	gear ratio		

For the identification, the entire valve was operated in closed-loop position control of the flap angle $\varphi_G(t)$. The setpoint and corresponding measurements are shown in Fig. 24.4. The signals have been sampled with a sampling frequency of 100 Hz. Furthermore, the measurements have been filtered with an FIR realized low-pass filter with $m = 24$ coefficients and a corner frequency of $f_C = 5$ Hz. The rotational velocity has been generated by a differentiating filter from the measurement of the rotational position.

Based on (24.1.1) and (24.1.2), one can now set up a parameter estimation problem. For the parameter estimation, the following measured and calculated signals are available: $U_A(t)$, $I_A(t)$, $\omega_R(t)$, and $\varphi_G(t)$. It was found that the time constant of the RL circuit was so small that the inductance L_A could not be estimated reliably with the given sample rate. Hence, the electric circuit was simplified to

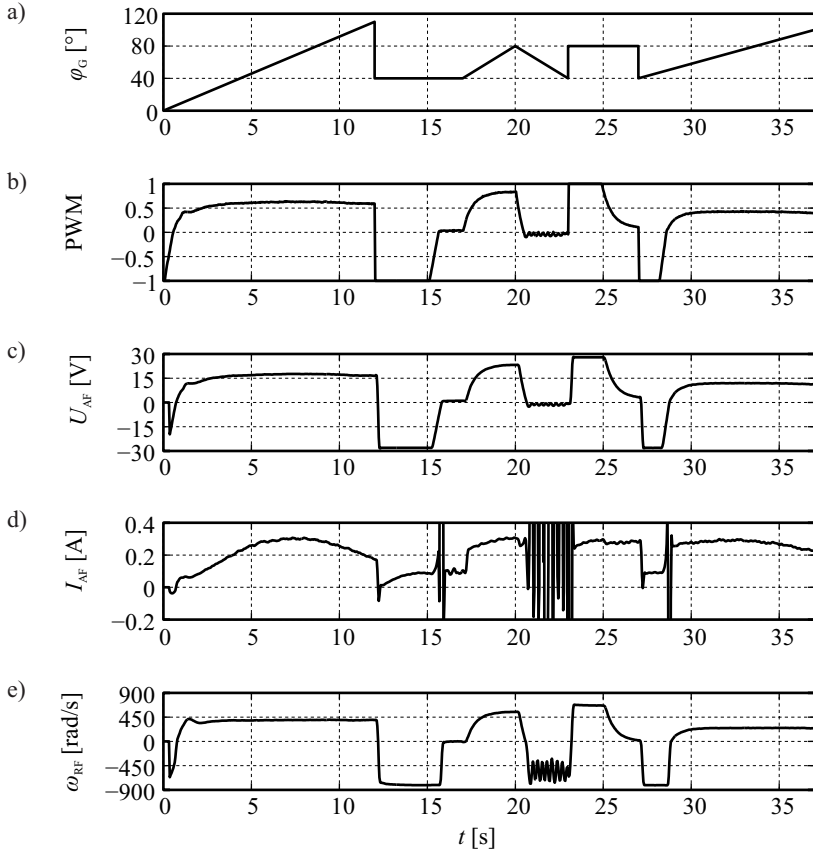


Fig. 24.4. Setpoint and measurements for the brushless DC motor. **(a)** setpoint flap angle, **(b)** PWM duty cycle, **(c)** filtered phase voltage, **(d)** filtered phase current, **(e)** filtered rotational velocity (Vogt, 1998)

$$U_A(t) = R_A I_A(t) + \Psi \omega_R(t) . \quad (24.1.5)$$

The signals were sampled and the model for the parameter estimation was then given as

$$y(k) = \psi^T(k) \theta \quad (24.1.6)$$

with

$$y(k) = U_A(k) \quad (24.1.7)$$

$$\psi^T(k) = (I_A(k) \ \omega_R(k)) \quad (24.1.8)$$

$$\theta = \begin{pmatrix} R_A \\ \Psi \end{pmatrix} , \quad (24.1.9)$$

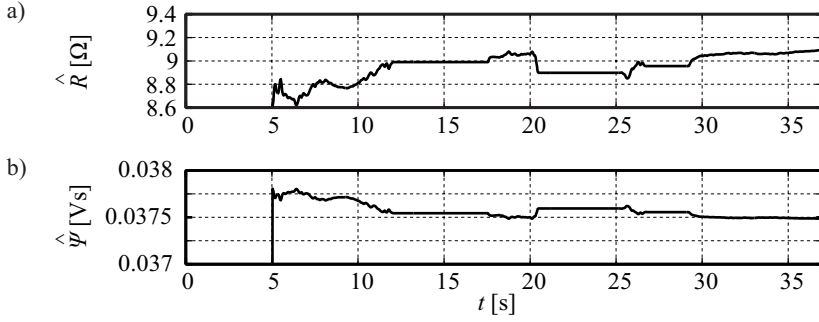


Fig. 24.5. Identification results for the brushless DC Motor. **(a)** Ohmic resistance, **(b)** magnetic flux linkage (Vogt, 1998)

allowing to provide the parameter estimates \hat{R}_A and $\hat{\psi}$ by means of the method of least squares.

Also, the magneto-mechanical system had to be simplified, resulting in the model

$$\Psi I_A(t) = J \frac{d}{dt} \omega_R(t) + M_C \text{sign } \omega_R + c_F \varphi_G(t) . \quad (24.1.10)$$

A few parameters were assumed to be known, including the rotational inertia and the load characteristics, leading to the model

$$y(k) = \psi^T(k) \theta \quad (24.1.11)$$

with

$$y(k) = \Psi I_A(k) - c_s \varphi_G(k) - J \dot{\omega}_R(k) \quad (24.1.12)$$

$$\psi^T(k) = (\text{sign } \omega_R(k)) \quad (24.1.13)$$

$$\theta = (M_C) , \quad (24.1.14)$$

which allowed to estimate the coefficient of Coulomb friction \hat{M}_C by means of the method of least squares. Hence, in total, three parameters \hat{R}_A , $\hat{\psi}$, and \hat{M}_C are estimated.

Various parameter estimation methods were applied like: RLS (recursive least squares), DSFI (discrete square root filtering), FDSFI (fast DSFI), NLMS (normalized least mean squares) and compared with regard to computational effort in floating point and integer word realization and estimation performance. The floating point implementation is standard for e.g. 16 bit signal processors and in this case RLS, DSFI, or FDSFI can be used. However, integer word implementation is (still) required if reliable and certified low cost microcontrollers like the 16 bit Siemens C167 have to be used. Then, only NLMS is feasible (Moseler, 2001).

The forgetting factor has been chosen as $\lambda = 0.999$. Not all measurements are evaluated for the parameter estimation as the model is not precise enough in certain operating regimes. The estimation algorithm employs only measurements from the

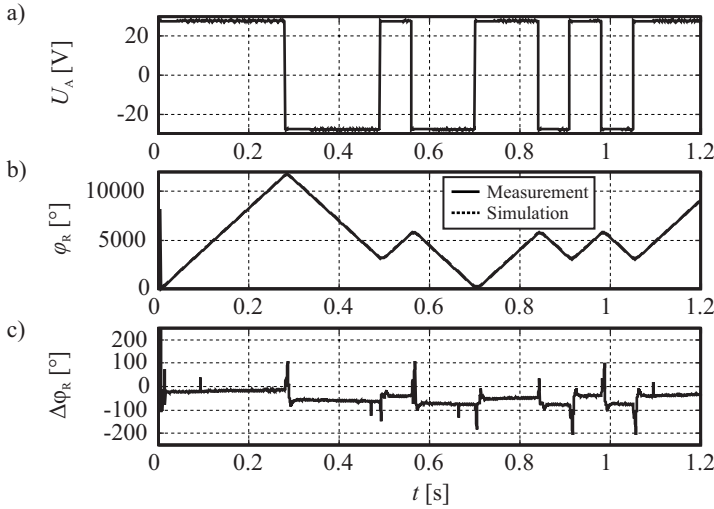


Fig. 24.6. Validation of the model. (a) phase voltage, (b) rotor angle, note that measured and simulated values lie almost on top of each other, (c) error between measured and simulated rotor angle (Vogt, 1998)

interval $0.05 \leq \text{PWM} \leq 0.95$ and $\omega > 10 \text{ rad/s}$. This also ensures that no division by zero can occur in the estimation equation. As FIR filters are used for noise cancellation, the filters can be switched off while no parameters are estimated. Whenever the measurements enter the corridor for parameter estimation, the first m samples are disposed. Upon the time step $m + 1$, the transient effects in the filter have died out and the filter output can safely be used for parameter estimation. The run of the estimated parameters is shown in Fig. 24.5. Furthermore, the first three seconds of the measurements have also been disposed to avoid falsification of the estimation results due to transients. The output of the parameter estimates starts at $t = 5 \text{ s}$ to ensure that the variance of the parameter estimates has already reduced to reasonable values. The high fidelity of the derived model is illustrated in Fig. 24.6. Here, the classical y - t plot has been used for validation of the results.

24.1.2 Electromagnetic Automotive Throttle Valve Actuator

Another example for parameter estimation applied to a DC drive with load is the automotive throttle valve actuator. Since about 1990, electrical driven throttle valves became a standard component for gasoline engines. They control the air mass flow through the intake manifold to the cylinders. The electric throttles are manipulated by the accelerator pedal sensors via an electronic control unit and additional control inputs from idle speed control, traction control, and cruise control. Here, in contrast to the previous example, a traditional DC motor with mechanical commutator is employed.

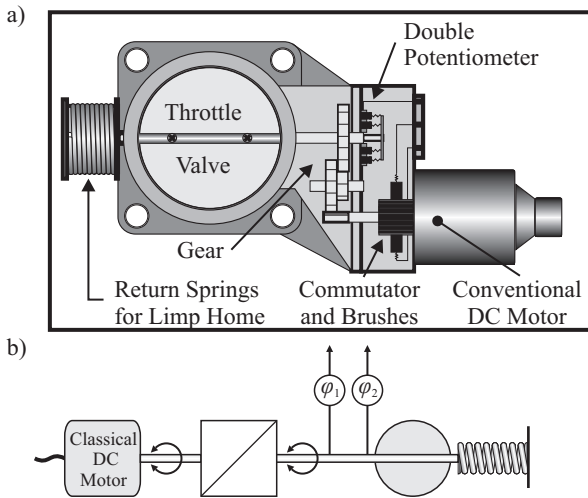


Fig. 24.7. (a) Scheme and (b) schematic block diagram of an electric throttle of a gasoline engine

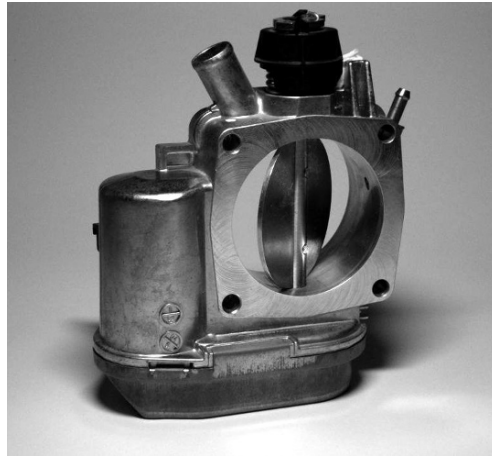


Fig. 24.8. Photo of an electric throttle of a vehicle

Figure 24.7 shows a schematic drawing of the actuator, a photo is shown in Fig. 24.8. A permanently excited DC motor with brush commutation drives the throttle through a two-stage gear in the opening or closing direction. It operates against the main helic spring. A second spring works in the closing region in the opposite direction, in order to open the throttle in the case of a voltage loss into a limp-home position (a mechanical redundancy). The motor is manipulated by a pulse width modulated (PWM) armature voltage $U_A \in (-12 \text{ V} \dots +12 \text{ V})$. The measured variables are the armature voltage U_A , the armature current I_A , and the angular throttle posi-

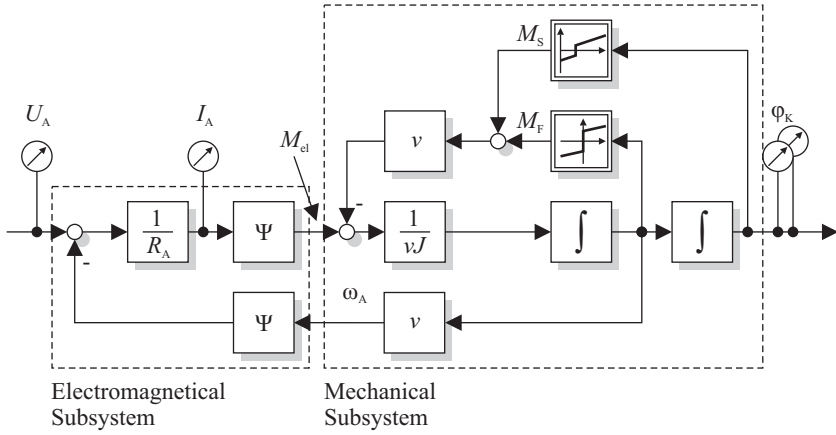


Fig. 24.9. Schematic of the DC drive with load

tion $\varphi_k \in (0^\circ \dots 90^\circ)$. This throttle position is measured by two redundant wiper-potentiometers operating in two different directions. The position controller was a model-based sliding-mode-controller or PID controller with time lag and sampling time $T_0 = 1.5$ ms (Pfeufer, 1997, 1999).

Theoretical modeling of the throttle valve leads to the following basic equations (Isermann, 2005). The DC motor is governed by

$$U_A(t) = R_A I_A(t) + \Psi \omega_A(t) \quad (24.1.15)$$

$$M_{el}(t) = \Psi I_A(t) , \quad (24.1.16)$$

while the mechanical part (related to the motor axle) can be modeled as

$$\nu J \dot{\omega}_k(t) = M_{el}(t) - M_{mech}(t) \quad (24.1.17)$$

$$M_{mech}(t) = \frac{1}{\nu} (c_{S1} \varphi_k(t) + M_{S0} + M_F) \text{ for } \varphi_k > \varphi_{k0} \quad (24.1.18)$$

$$M_F(t) = M_{F0} \text{sign } \omega_k(t) + M_{F1} \omega_k(t) \quad (24.1.19)$$

In this example, the used symbols are:

R_A	armature resistance	Ψ	magnetic flux linkage
ν	gear ratio ($\nu = 16.42$)	J	moment of inertia of the motor
M_{F0}	Coulomb friction torque	M_{F1}	viscous friction torque
c_{S1}	spring constant	M_{S0}	spring pretension
ω_k	throttle angular speed ($= \dot{\varphi}_k$)	ω_A	motor angular speed, $\omega_A = \nu \omega_k$

The armature inductance can be neglected, because the electrical time constant $M_{el} = L_A/R_A \approx 1$ ms is much smaller than the mechanical dynamics. Depending on the input excitation either the Coulomb friction or the viscous friction turned out to be dominant when measurements were taken at a testbed.

Parameter Estimation for the Dynamic Behavior

The parameter estimation is carried out with recursive least squares estimation in the form of discrete square root filtering (DSFI). The basic model equation is

$$y(t) = \psi^T(t)\theta \quad (24.1.20)$$

and the data vector and the parameter estimation for the electrical part are

$$y(t) = U_A(t) \quad (24.1.21)$$

$$\psi^T(t) = (I_A(t) \ v \omega_k(t)) \quad (24.1.22)$$

$$\theta = \begin{pmatrix} \theta_1 \\ \theta_2 \end{pmatrix} \quad (24.1.23)$$

and for the mechanical part

$$y(t) = \dot{\omega}_k(t) \quad (24.1.24)$$

$$\psi^T(t) = (I_A(t) \ \varphi_k(t) \ \omega_k(t) \ 1) \quad (24.1.25)$$

$$\theta = \begin{pmatrix} \theta_4 \\ \theta_5 \\ \theta_6 \\ \theta_7 \end{pmatrix} \quad (24.1.26)$$

Because of a fast input excitation, the Coulomb friction term is neglected and only the viscous friction parameter M_{F1} is estimated under the condition that the speed is sufficiently large, i.e. $|\omega_k| > 1.5 \text{ rad/s}$.

The relation between the physical process coefficients and the parameter estimates are

$$\begin{aligned} \hat{\theta}_1 &= R_A, \quad \hat{\theta}_2 = \Psi, \\ \hat{\theta}_4 &= \frac{\Psi}{vJ}, \quad \hat{\theta}_5 = -\frac{c_{S1}}{v^2J}, \quad \hat{\theta}_6 = -\frac{M_{F1}}{v^2J}, \quad \hat{\theta}_7 = -\frac{M_{S0}}{v^2J} \end{aligned} \quad (24.1.27)$$

As the gear ratio v is known, the rotational inertia follows from

$$J = \frac{\hat{\theta}_2}{v\hat{\theta}_4} \quad (24.1.28)$$

All other process coefficients can directly be determined from the parameter estimates $\hat{\theta}_i$.

For the parameter estimation, the actuator operates in closed loop and the setpoint is changed with a PRBS signal between 10° and 70° . The derivatives $\omega_k = \dot{\phi}_k$ and $\dot{\omega}_k = \ddot{\phi}_k$ are determined by a state variable filter with the sampling time chosen as $T_{O,SVF} = 2 \text{ ms}$. The sampling time for the parameter estimation is $T_0 = 6 \text{ ms}$. The resulting parameter estimates converge fast and the largest equation error is $\leq 5\%$ or $\leq 3.5^\circ$ for the electrical part and $\leq 7 \dots 12\%$ for the mechanical part (Pfeufer, 1999).

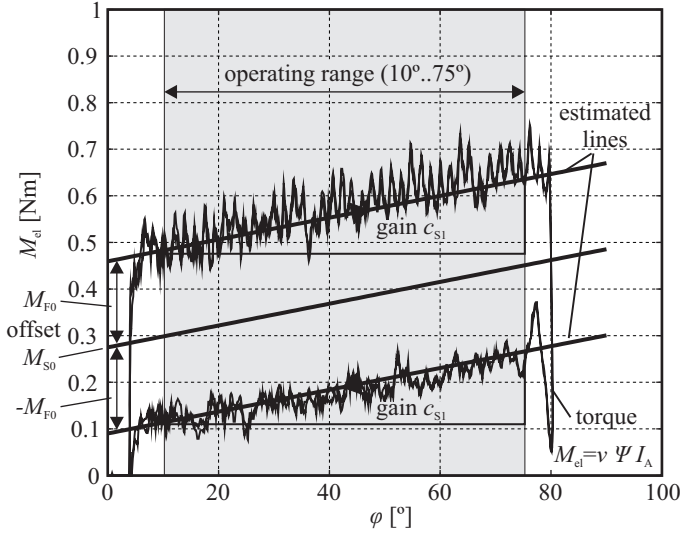


Fig. 24.10. Estimated static behavior of the throttle actuator

Parameter Estimation for the Static Behavior

In order to obtain more precise information about the mechanical part and especially the friction phenomena, only the static behavior is considered for slow continuous input changes.

Setting $\dot{\omega}_k = 0$ and neglecting the viscous friction, (24.1.15) to (24.1.19) yield with $t = kT_0$

$$I_A(k) = \frac{1}{\nu\Psi} (c_{S1}\varphi_k(k) + M_{S0} + M_{F0} \text{sign } \omega_k(k)) = \psi^T(k)\theta \quad (24.1.29)$$

Because of the direction-dependent Coulomb friction for the opening and closing, two separate estimations are made

$$\psi_1^T(k) = (\varphi_k^+(k) \ 1), \quad \psi_2^T(k) = (\varphi_k^-(k) \ 1)$$

$$\hat{\theta}^+(k) = \begin{pmatrix} \hat{\theta}_1 \\ \hat{\theta}_2 \end{pmatrix} \quad \hat{\theta}^-(k) = \begin{pmatrix} \hat{\theta}_3 \\ \hat{\theta}_4 \end{pmatrix}$$

with

$$\begin{aligned} \hat{\theta}_1 &= \frac{c_{S1}}{\nu\Psi} & \hat{\theta}_2 &= \frac{M_{S0}}{+} M_{F0} \nu\Psi \\ \hat{\theta}_3 &= \frac{c_{S1}}{\nu\Psi} & \hat{\theta}_4 &= \frac{M_{S0} - M_{F0}}{\nu\Psi} \end{aligned}$$

The magnetic flux linkage Ψ is known from (24.1.27). The physical process parameters then result as

$$c_{S1} = \nu \Psi \frac{\hat{\theta}_1 + \hat{\theta}_3}{2}$$

$$M_{S0} = \nu \Psi \frac{\hat{\theta}_2 + \hat{\theta}_4}{2}$$

$$M_{F0} = \nu \Psi \frac{\hat{\theta}_2 - \hat{\theta}_4}{2}$$

The parameter estimation is performed with recursive DSFI and the sample time $T_0 = 6$ ms for each motion. Figure 24.10 shows the resulting friction characteristics. The spring pretension M_{S0} leads to a positive offset of the linear spring characteristic and the dry friction shifts the friction characteristic by M_{F0}^+ and M_{F0}^- such that a hysteresis characteristic results. A comparison with the electrical torque $M'_{el} = \nu \Psi I_A$ related to the throttle axle indicates a good agreement with the estimated hysteresis characteristic. (The oscillations of the calculated electrical torque are due to the closed loop behavior in connection with adhesive friction or stick-slip effects, which are not modeled. The range around the point of return, where adhesion works, is omitted in the parameter estimation for simplifying reasons).

24.1.3 Hydraulic Actuators

Hydraulic systems are used in manifold applications. They excel especially whenever there is a need for high power density combined with fast actuation capabilities. Furthermore, hydraulic cylinders can easily generate linear motions, whereas e.g. electric motors typically need a conversion gear to generate a linear motion.

Introduction

The typical setup of a hydraulic servo axis is shown in Fig. 24.11: A positive displacement pump acts as a pressure supply. Oil is drawn from a supply tank and is expelled at high pressure into the supply line. From there, the oil flows to the individual hydraulic servo axes, which in the case of a linear motion, typically consist of a proportional acting valve and a hydraulic cylinder. The valve is used to throttle the hydraulic flow and direct it into one of the two chambers of the hydraulic cylinder. For this task, the valve contains a so-called *valve spool*, which can move freely inside the *valve sleeve*. The valve spool can be driven by a variety of forces. By the hand force of a worker (e.g. construction machinery), by a hydraulic force (e.g. second stage of a two-stage valve), by a torque motor (e.g. nozzle-flapper unit of the first stage of a two stage valve), or, as in the case at hand, by the force of two solenoids (direct-driven valve), see Fig. 24.13. As the valve spool moves tiny openings occur and a turbulent flow evolves according to the pressure drop Δp across the tiny opening. The oil flows into the hydraulic cylinder and exerts a pressure on the piston. By means of the piston rod, this force is transferred to drive an external load. As the piston moves, oil from the opposite chamber is pushed back into the supply tank. The two cylinder chambers thus have to be isolated by the piston. Here, one typically uses the setup depicted in Fig. 24.14 for standard hydraulic cylinders. Here,

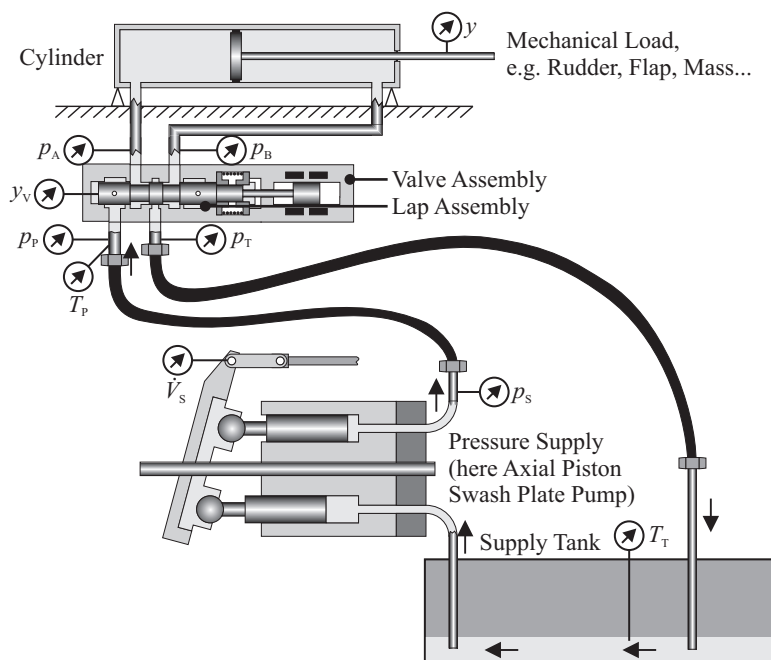


Fig. 24.11. Scheme of a hydraulic servo axis

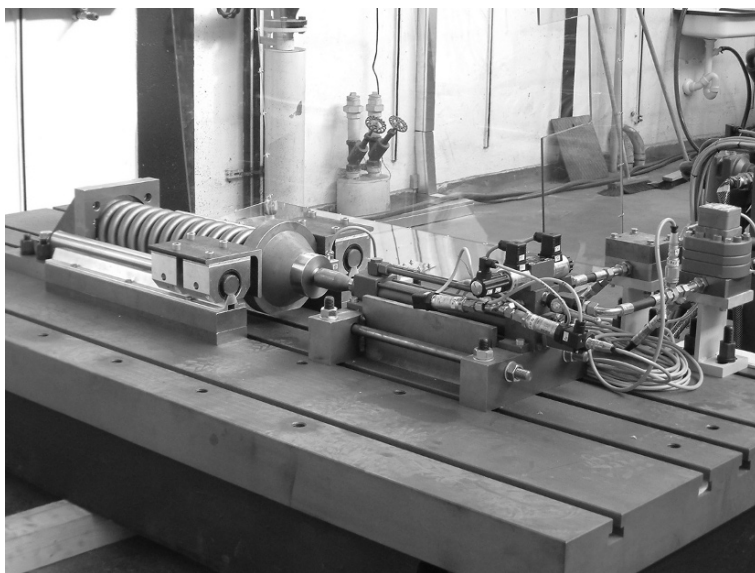


Fig. 24.12. Photo of the hydraulic servo axis testbed

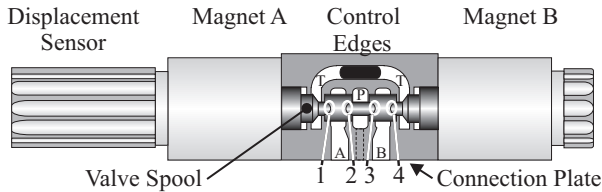


Fig. 24.13. Schematic view of a direct-driven proportional acting valve and control edge numbering

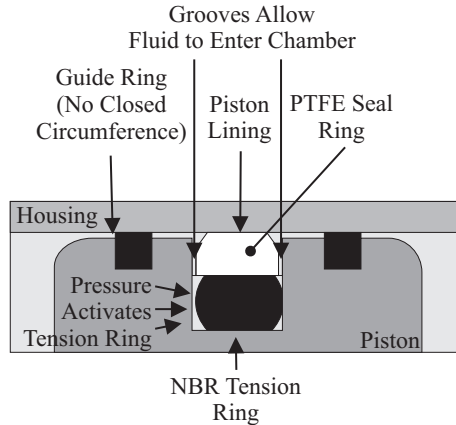


Fig. 24.14. Schematic of the cylinder sealing isolating the two cylinder chambers

one has to obey a certain trade-off: If the cylinder sealing is pushed tightly against the cylinder housing, it would wear out very fast as the piston constantly moves and hence friction will occur between the sealing and the cylinder housing. On the other side, if the sealing is fitted too loosely, a large bypass flow between the two cylinder chambers will result as a combined pressure induced and adhesion induced flow will result. Especially in the area of fault detection and diagnosis, one is interested in determining the coefficient of leakage flow, as it is a good indicator of the sealing health. The measurements and results that are presented in this section stem from the hydraulic servo axis testbed shown in Fig. 24.12. Some technical data are listed in Table 24.3.

Here and in the remainder of this section, the following symbols are used:

b_V	coefficient of valve flow	A_A	active piston area chamber A
V_{0A}	dead volume chamber A	G_{AB}	laminar leakage coefficient
E_{0A}	bulk modulus chamber A	\dot{V}	volume flow rate
T	fluid temperature	\dot{V}_A	flow rate into chamber A
y_V	valve spool displacement	y	piston displacement
p_A	pressure in chamber A	k	spring stiffness of load
m	mass of load	F_0	Coulomb friction force

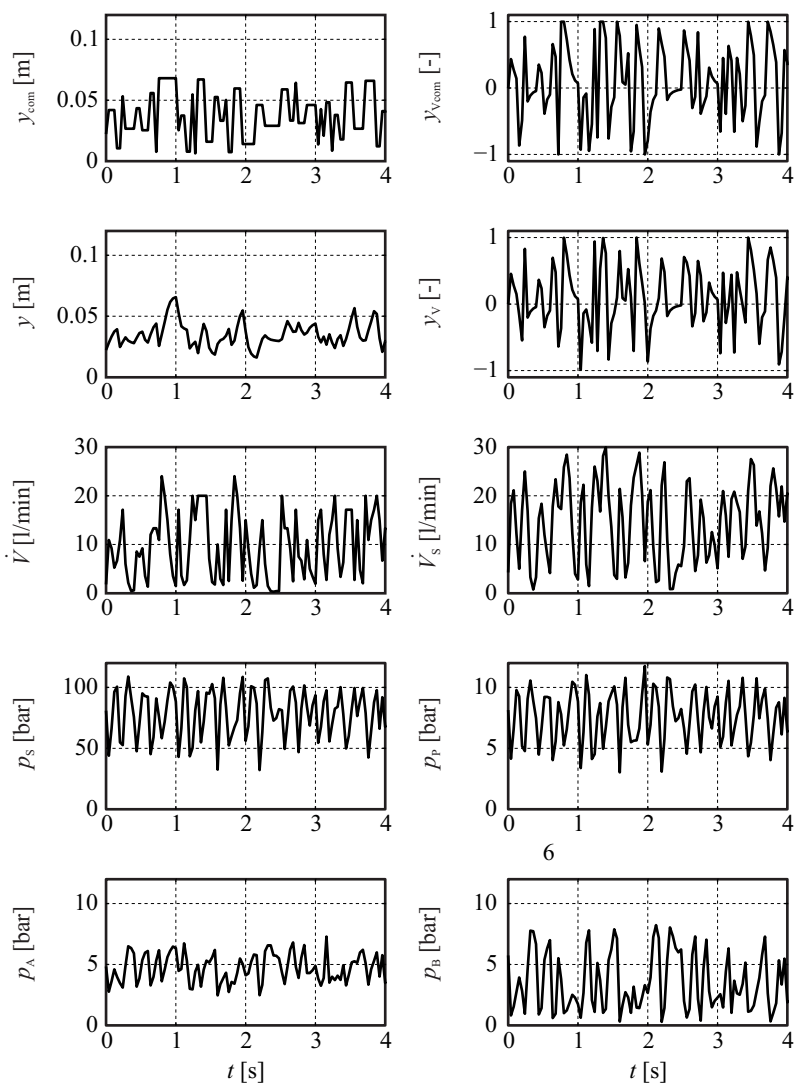


Fig. 24.15. Measurements taken at the hydraulic servo axis. For the sensor location, see Fig. 24.11

Table 24.3. Specifications of the hydraulic servo axis shown in Fig. 24.12 operating with HLP46 as hydraulic oil

Parameter	Value
System pressure	80 bar
Max. pressure supplied by pump	280 bar
Pump displacement	45 cm ³ /rev
Cylinder diameter	40 mm
Piston rod diameter	28 mm
Cylinder stroke	300 mm
Max. velocity	1 m/s
Max. force	20 kN
Mass of load	40 kg
Spring stiffness of load	100 000 N/m
Density of fluid at 15°C	0.87 g/cm ³
Mean bulk modulus of fluid	2 GPa

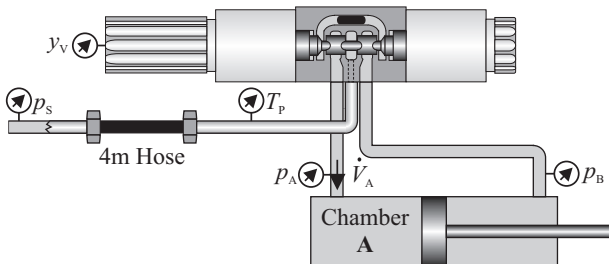


Fig. 24.16. Schematic view of a direct-driven proportional acting valve and hydraulic cylinder

c coefficient of viscous friction

The index denote the following:

A	cylinder chamber A	B	cylinder chamber B
P	pressure line	T	return line or tank
S	pressure supply / pump		

For the sensor location, see Figs. 24.11 and 24.16. A measurement recorded at the hydraulic servo axis is shown in Fig. 24.15.

Identification of the Hydraulics

The flow over the control edge is given as

$$\dot{V}(t) = b_v(y_v(t), T(t)) \sqrt{|\Delta p(t)|} \text{sign } \Delta p(t) . \quad (24.1.30)$$

One can see that the coefficient of the flow b_v depends on both the valve spool displacement $y_v(t)$ as well as the fluid temperature. The flow balance for e.g. chamber

A of the hydraulic cylinder is given as

$$\dot{V}_A(t) = A_A \dot{y}(t) - G_{AB}(p_A(t) - p_B(t)) - \frac{1}{E_{0A}}(V_{0A} + A_A y(t)) \dot{p}_A(t) . \quad (24.1.31)$$

For identification purposes, the following signals will be utilized: $y_V(t)$ valve spool displacement, $p_A(t)$ pressure in chamber A, $p_B(t)$ pressure in chamber B, $p_S(t)$ pressure at the supply, $y(t)$ position of the piston. The fluid temperature $T(t)$ is measured, but can be neglected depending on the requirements of the model fidelity.

The valve opening characteristics $b_V(y_V)$ are due to their non-linear behavior modeled as a polynomial as

$$b_{Vi}(y_V) = b_{V1i} y_V(t) + b_{V2i} y_V^2(t) + b_{V3i} y_V^3(t) , \quad (24.1.32)$$

where the index i denotes the control edge to be modeled, see Fig. 24.13 for the numbering of the control edges. As there are four possible flow paths, there will also be four independent polynomials.

The individual models will now be combined. This yields

$$\begin{aligned} (V_{0A} + A_A y(t)) \frac{1}{\bar{E}(T)} \dot{p}_A(t) + A_A \dot{y}(t) = \\ \dot{V}_{PA}(p_A, p_P, T, y_V) - \dot{V}_{AT}(p_A, T, y_V) - G_{AB}(T)(p_A(t) - p_B(t)) \end{aligned} \quad (24.1.33)$$

with

$$\dot{V}_{PA}(p_A, p_S, T, y_V) = b_{V2}(y_V, T) \sqrt{|p_S(t) - p_A(t)|} \text{sign}(p_P(t) - p_A(t)) \quad (24.1.34)$$

$$\dot{V}_{AT}(p_A, T, y_V) = b_{V1}(y_V, T) \sqrt{|p_A(t)|} \text{sign } p_A(t). \quad (24.1.35)$$

These equations can be combined into one model. Since parameter estimation is based on sampled signals, the time t will now be expressed as integer multiples k of a fixed sampling time T_0 . The model for chamber A is given as

$$(V_{0A} + A_A y(k)) \frac{1}{\bar{E}(T_P)} \dot{p}_A(k) + A_A \dot{y}(k) = (\dot{V}_A(p_A, p_S, T_P, y_V) - \dot{V}_{AB}(p_A, p_B, T_P)) , \quad (24.1.36)$$

where \bar{E} is the mean bulk modulus. The valve flow with a polynomial approximation of the valve flow characteristics is given as

$$\begin{aligned} \dot{V}_A(p_A, p_S, T_P, y_V) = & \left(\sum_{i=k}^l b_{1i}(T_P) y_V(k)^i \right) \sqrt{|\Delta p_{SA}(k)|} \text{sign } \Delta p_{SA}(k) \\ & - \left(\sum_{i=k}^l b_{2i}(T_P) y_V(k)^i \right) \sqrt{|\Delta p_{AT}(k)|} \text{sign } \Delta p_{AT}(k) \end{aligned} \quad (24.1.37)$$

where $\Delta p_{SA}(k) = p_S(k) - p_A(k)$ and $\Delta p_{AT}(k) = p_A(k)$. The internal leakage is given as

$$\dot{V}_{AB}(p_A, p_B, T_P) = G_{AB}(T_P)(p_A(k) - p_B(k)) . \quad (24.1.38)$$

Combining the above equations and solving for $\dot{y}(k)$ yields

$$\dot{V}_A(p_A, p_S, T, y_V) - G_{AB}(T)(p_A(k) - p_B(k)) - \frac{(V_{0A} + A_A y(k))}{\bar{E}(T)} \dot{p}_A(k) = A_A \dot{y}(k) \quad (24.1.39)$$

Now, the valve flow can be inserted. The polynomial will be written out to see that this parameter estimation problem is truly linear in parameters,

$$\begin{aligned} & \dots + b_{1i}(T) y_V(k)^i \sqrt{|\Delta p_{SA}(k)|} \text{sign}(\Delta p_{SA}(k)) (y_V(k) \geq 0) + \dots \\ & - \dots - b_{2i}(T) y_V(k)^i \sqrt{|\Delta p_{AT}(k)|} \text{sign}(\Delta p_{AT}(k)) (y_V(k) < 0) - \dots \\ & - G_{AB}(T)(p_A(k) - p_B(k)) - \frac{(V_{0A} + A_A y(k))}{\bar{E}(T)} \dot{p}_A(k) = A_A \dot{y}(k) \end{aligned} \quad (24.1.40)$$

where the terms $(y_V(k) \geq 0)$ and $(y_V(k) < 0)$ amount to one if the corresponding condition is fulfilled and are zero otherwise.

This entire parameter estimation problem now can be split up into the data matrix

$$\Psi^T = \begin{pmatrix} \vdots & & & & \\ y_V(k)^i \sqrt{|\Delta p_{SA}(k)|} \text{sign}(\Delta p_{SA}(k)) \cdot (y_V(k) \geq 0) & \dots & & & \\ \vdots & & & & \\ y_V(k)^i \sqrt{|p_A(k)|} \text{sign } p_A(k) \cdot (y_V(k) < 0) & \dots & & & \\ \vdots & & & & \\ p_A(k) - p_B(k) & \dots & & & \\ A_A y(k) \dot{p}_A(k) & \dots & & & \end{pmatrix} \quad (24.1.41)$$

and the output vector

$$y^T = (A_A \dot{y}(k), \dots). \quad (24.1.42)$$

The solution of the parameter estimation problem supplies estimates for the parameter vector θ given as

$$\hat{\theta}^T = \left(\hat{b}_{10}(T) \dots \hat{b}_{1n}(T) \hat{b}_{20}(T) \dots \hat{b}_{2n}(T) \dots \hat{G}_{AB}(T) \frac{1}{\hat{E}(T)} \right). \quad (24.1.43)$$

This parameter vector contains $2n + 2$ variables. Although such a parameter estimation problem can easily be solved on modern computers, it will only be used for offline identification. For online identification, the parameter estimation problem is split: Two independent parameter estimation problems for $y_V(k) \geq 0$ and $y_V(k) < 0$ are formulated to constrain the number of parameters to be estimated in each iteration. Since the valve spool displacement can only be positive or negative at any instant in time, the parameter estimation problem can be simplified.

The results of the parameter estimation can be seen in Fig. 24.17 and Fig. 24.18. Figure 24.17 shows that the non-linear behavior of the valve flow coefficient as a

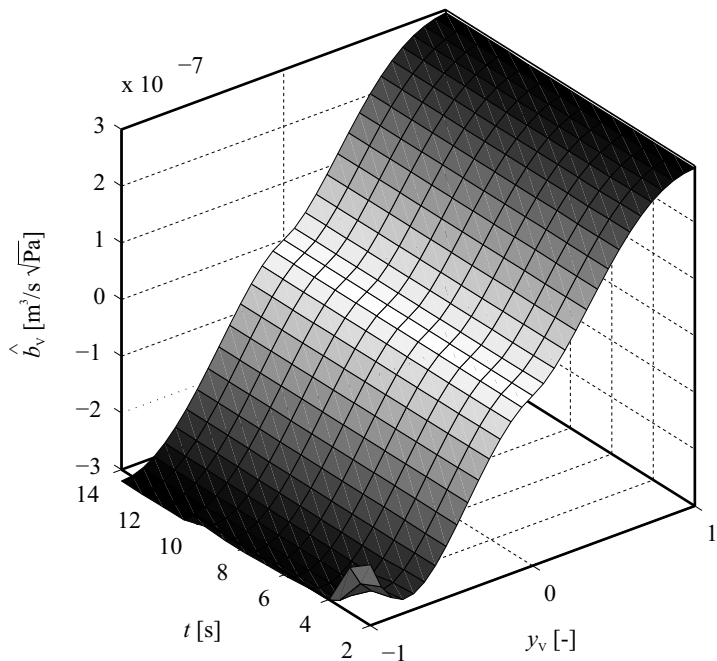


Fig. 24.17. Estimation of non-linear valve characteristics b_V over time. Note that the valve characteristics are non-linear and have been approximated by a polynomial in y_V . The modeled control edges are $P \rightarrow A$ for positive values of y_V and $T \rightarrow A$ for negative values of y_V

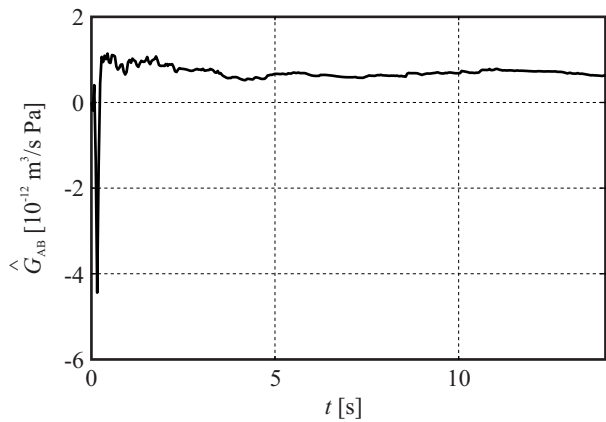


Fig. 24.18. Estimation of laminar leakage coefficient G_{AB} over time

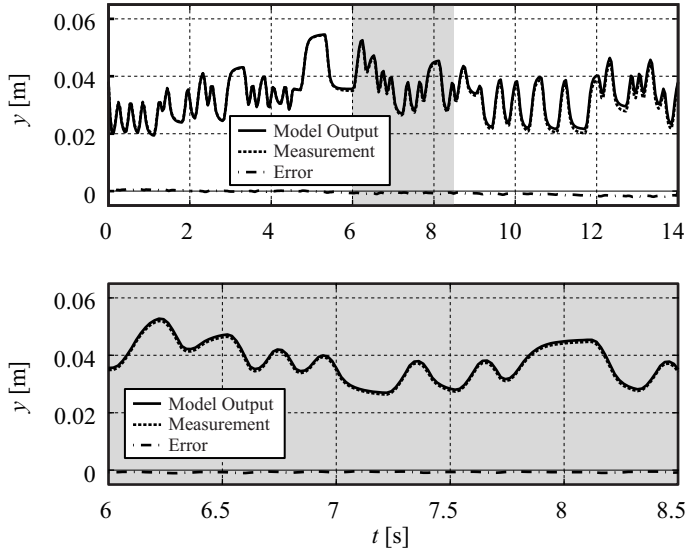


Fig. 24.19. Simulation of the hydraulic subsystem of the hydraulic servo axis

function of the valve opening is identified very well. The identification results of the laminar leakage coefficient in Fig. 24.18 also match very well with the values reported in literature. As was stated in the introduction to this section, knowledge of the laminar leakage coefficient is of special interest in the area of fault detection and diagnosis. Finally, Fig. 24.19 shows a simulation run and comparison with measurements. One can see that the model that has been parameterized by measurements shows a very good model fidelity. This high model fidelity can in large part be attributed to the nonlinear modeling of the valve characteristics.

Hydraulic servo axes typically operate with a large variety of loads. Furthermore, the load can change drastically during operation. To be able to maintain a good control quality despite the large variations in the load and hence the plant parameters, one can use adaptive control algorithms (e.g. Isermann et al, 1992). To be able to update the controller, one needs a good model of the load. Hence, the load driven by the hydraulic servo axis will now be identified based on sensors mounted at the hydraulic servo axis, see Fig. 24.20.

A general load model is shown in Fig. 24.21. This model covers both a mass and a spring as a load and also contains friction effects, which are modeled as a combination of Coulomb and viscous friction. It should be mentioned that even though results have been obtained for a spring-mass load only, the methods will apply to all kinds of loads which can be described by the general load model given in (24.1.44) and Fig. 24.21.

With the piston as the force-generating element of the hydraulic servo axis, the mechanics can be described in general form by

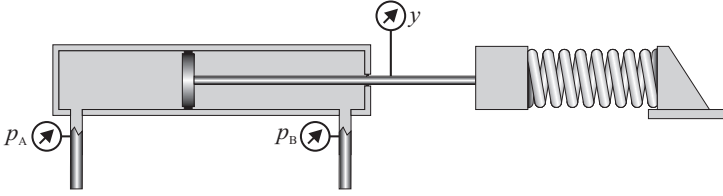


Fig. 24.20. Scheme of the mechanical load consisting of spring and mass

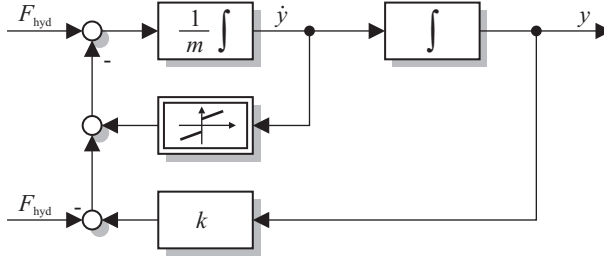


Fig. 24.21. Block diagram of the mechanical load model consisting of spring and mass

$$p_A(t)A_A - p_B(t)A_B = k(y(t) - y_0) + m\ddot{y}(t) + \begin{cases} -F_0 + c^-\dot{y}(t) & \text{for } \dot{y}(t) < 0 \\ F_0 + c^+\dot{y}(t) & \text{for } \dot{y}(t) \geq 0 \end{cases}, \quad (24.1.44)$$

where the friction force $F_F(\dot{y}(t))$ is a combination of Coulomb friction and viscous friction. F_0 is the static friction force and c^- and c^+ are the direction-dependent coefficients of viscous friction.

(24.1.44) is the basis for the parameter estimation problem. The spring pretension is estimated by the spring pre-compression displacement y_0 . Based on this equation, the data matrix of the parameter estimation problem becomes

$$\Psi = \begin{pmatrix} y(1) & 1 & \ddot{y}(1) & \text{sign } \dot{y}(1) & \dot{y}(1) \cdot (\dot{y}(1) > 0) & \dot{y}(1) \cdot (\dot{y}(1) < 0) \\ y(2) & 1 & \ddot{y}(2) & \text{sign } \dot{y}(2) & \dot{y}(2) \cdot (\dot{y}(2) > 0) & \dot{y}(2) \cdot (\dot{y}(2) < 0) \\ \vdots & \vdots & \vdots & \vdots & \vdots & \vdots \\ y(N) & 1 & \ddot{y}(N) & \text{sign } \dot{y}(N) & \dot{y}(N) \cdot (\dot{y}(N) > 0) & \dot{y}(N) \cdot (\dot{y}(N) < 0) \end{pmatrix}. \quad (24.1.45)$$

The output vector is

$$y = \begin{pmatrix} p_A(1)A_A - p_B(1)A_B \\ p_A(2)A_A - p_B(2)A_B \\ \vdots \\ p_A(N)A_A - p_B(N)A_B \end{pmatrix}. \quad (24.1.46)$$

The parameter of estimated quantities becomes

$$\theta^T = (\hat{k} \ (\hat{k} \cdot \hat{y}_0) \ \hat{m} \ \hat{F}_0 \ \hat{c}^- \ \hat{c}^+). \quad (24.1.47)$$

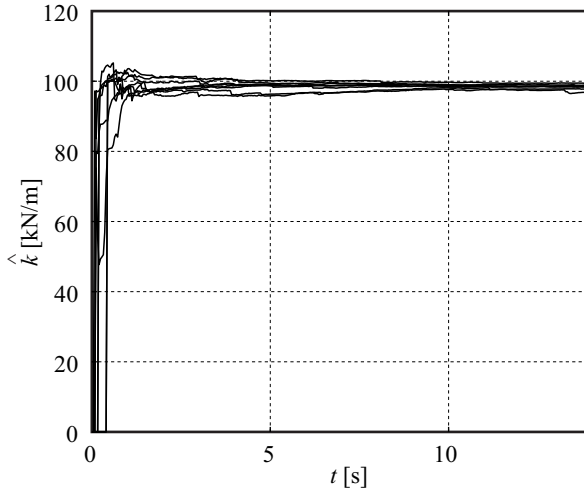


Fig. 24.22. Estimation of spring constant \hat{k} in several test runs

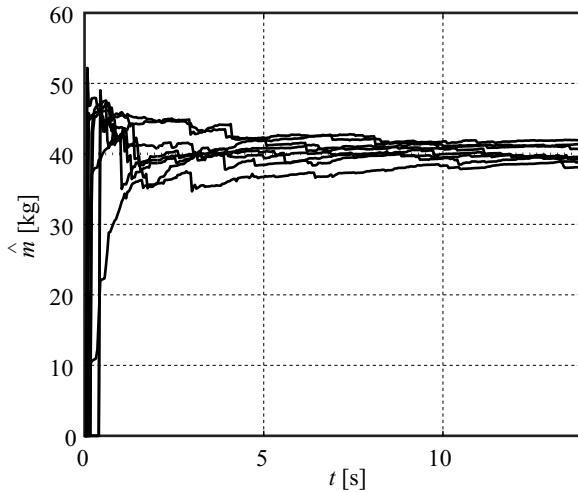


Fig. 24.23. Estimation of load mass \hat{m} in several test runs

With this parameter estimation method, the results depicted in Figs. 24.22 and 24.23 have been obtained. Recalling from the specifications in Table 24.3 and knowing that the mass of load was $m = 40 \text{ kg}$ and the spring stiffness $k = 100\,000 \text{ N/m}$, one can see that the estimates match well with the real values. One can once again run the model in parallel to the measurements to judge the quality of the identification results. This has been done in Fig. 24.24.

The identification method used was DSFI, the sample rate was $f_s = 500 \text{ Hz}$. The first and second derivative of the piston displacement were calculated directly as

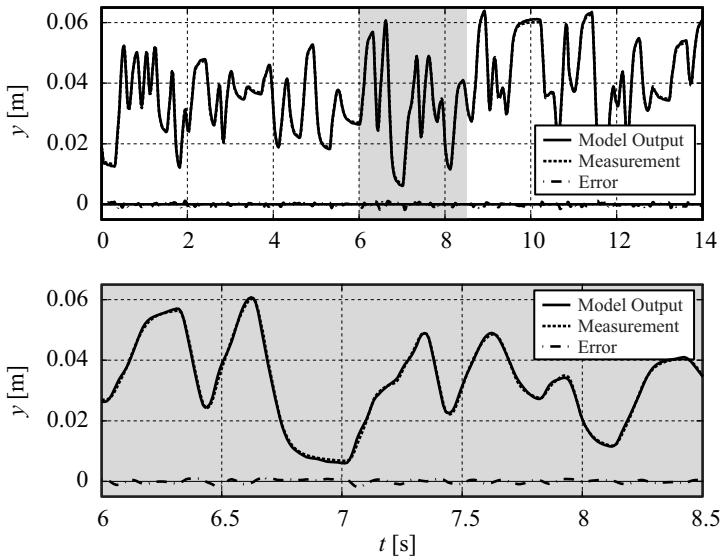


Fig. 24.24. Simulation of the mechanic subsystem of the hydraulic servo axis

the signal was supplied by a digital sensor and had little noise. For this, the central difference quotient was used to ensure that the measurements are not delayed. All methods were implemented as recursive parameter estimation to be able to follow changes of the plant e.g. for fault detection and diagnosis.

The detailed description of these parameter estimation approaches is covered in the dissertation by Muenchhof (2006). There, also the identification using neural nets has been discussed as well as the application of these identification techniques for fault detection and diagnosis.

24.2 Machinery

In the following, the application of identification methods to machinery will be treated. Here, the application of these methods can be advantageous for controller design, adaptive control, up to automatic commissioning of the machines as well as condition monitoring.

24.2.1 Machine Tool

As an example for a main drive, a machining center of type (MAHO MC5) is considered. A speed-controlled DC motor drives a belt, a gear and tool spindle, carrying a cutter or drill. Hence, a multi mass-spring-damper system results with 6 masses. A view of the main drive is shown in Fig. 24.25.

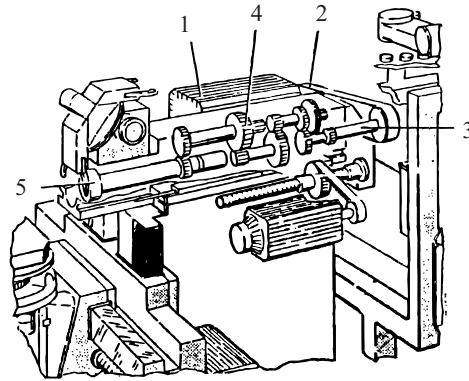


Fig. 24.25. Main drive of machining center MAHO MC5

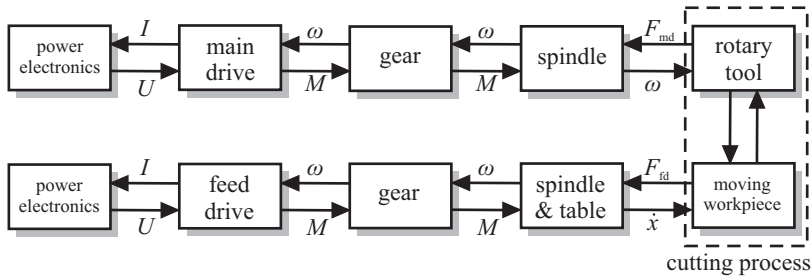


Fig. 24.26. Two-port representation of the signal flow of the main drive and one feed drive of a drilling or milling machine tool

In the following, small deviations of the variables are considered such that linear models can be assumed. The dynamic behavior of the DC motor is like in the previous examples modeled by

$$L_A \frac{d}{dt} I_A(t) = -R_A I_A(t) - \Psi \omega_1(t) + U_A(t) \quad (24.2.1)$$

$$J_1 \frac{d}{dt} \omega_1(t) = -\Psi I_A(t) - M_1(t) \quad (24.2.2)$$

with

L_A	armature inductance	U_A	armature voltage
R_A	armature resistance	I_A	armature current
Ψ	magnetic flux linkage	ω_1	motor speed ($\omega_1 = \dot{\varphi}$)
J_1	moment of inertia	M_1	load torque

An analysis of the eigenfrequencies of the main drive shows that the motor is able to excite frequencies in open loop $f < 80$ Hz and in closed loop $f < 300$ Hz (Wanke and Isermann, 1992). The eigenfrequency of the belt drive is 123 Hz and

those of shaft, gear, and spindle are 706, 412, and 1335 Hz. Hence, the dynamic behavior of the main drive is dominated by the motor and the belt drive and can therefore be modeled by a two-mass system with moment of inertias J_1 (motor plus belt driving pulley) and J_2 (belt driven pulley, shaft, gear, spindle). The mechanical part of the main drive is then described by a linear state space model

$$\dot{\mathbf{x}}(t) = \mathbf{A}\mathbf{x}(t) + \mathbf{b}u(t) + \mathbf{F}z(t) \quad (24.2.3)$$

with

$$\mathbf{x}^T(t) = (I_A(t) \varphi_1(t) \dot{\varphi}_1(t) \dots \varphi_5(t) \dot{\varphi}_5(t)) \quad (24.2.4)$$

$$u(t) = U_A(t) \quad (24.2.5)$$

$$\mathbf{z}^T(t) = (M_6(t) M_F(t)) \quad (24.2.6)$$

with M_6 being the load torque and M_F the Coulomb friction torque.

The parameters of the main drive can of course be determined from construction data. However, if not all parameters can be determined or for fault detection in normal operation, the estimation of the parameters from measured signals is desired.

To estimate the parameters of the main drive in idle running ($M_6 = 0$) based on measurements of accessible signals $U_A(t)$, $I_A(t)$, $\omega_1(t)$, and spindle speed $\omega_5(t)$, the following equations are used:

$$\begin{aligned} U_A(t) &= \theta_1 \omega_1(t) + \theta_2 I_A(t) + \theta_3 \dot{I}_A(t) \\ \theta_1 I_A(t) - M_R(t) &= \theta_4 \dot{\omega}_1(t) + \theta_5 \dot{\omega}_5(t) \\ \omega_5(t) &= \theta_6 \dot{\omega}_1(t) + \theta_7 \omega_1(t) - \theta_8 \dot{\omega}_5(t) - \theta_9 \ddot{\omega}_5(t) \end{aligned} \quad (24.2.7)$$

with

$$\begin{aligned} \theta_1 &= \Psi \quad \theta_2 = R_A \quad \theta_3 = L_A \\ \theta_4 &= J_1 \quad \theta_5 = i J_2 \quad \theta_6 = d i / c \\ \theta_7 &= i \quad \theta_8 = d / c \quad \theta_9 = J_2 i^2 / c \end{aligned} \quad (24.2.8)$$

The armature flux linkage is estimated by the first equation in (24.2.7) beforehand (or known from the data sheet). Then all process coefficients can be determined

$$\begin{aligned} i &= \theta_7 \text{ (gear ratio)} & c &= \theta_5 \theta_7 / \theta_9 \\ J_1 &= \theta_4 \text{ (motor)} & d &= \theta_5 \theta_7 \theta_8 / \theta_9 \\ J_2 &= \theta_5 / \theta_7 \text{ (spindle)} \end{aligned} \quad (24.2.9)$$

The derivatives of first and second order for continuous-time parameter estimation were determined with state variable filters designed as Butterworth filters of 6th order with corner frequencies of 79.6 Hz and 47.8 Hz. The resolution of the incremental rotation sensors was increased to 4096 slots for the spindle and 1024 slots for the motor. Sampling time was $T_0 = 0.5$ ms. The results with the parameter estimation method DSFI (discrete square root filtering information from 40 step functions of the speed over a time interval of 15 s are shown in Figs. 24.27 to 24.30.

The estimated motor coefficients on the motor side $\hat{\Psi}$, \hat{R}_A , and \hat{L}_A converge very fast within about 2 s, the mechanical coefficients \hat{J}_1 , \hat{J}_2 , \hat{c} , and \hat{d} a bit slower within about 5 s. After about 15 s all 8 process coefficients converge to steady state values and agree relatively well with theoretical determined values (Wanke, 1993).

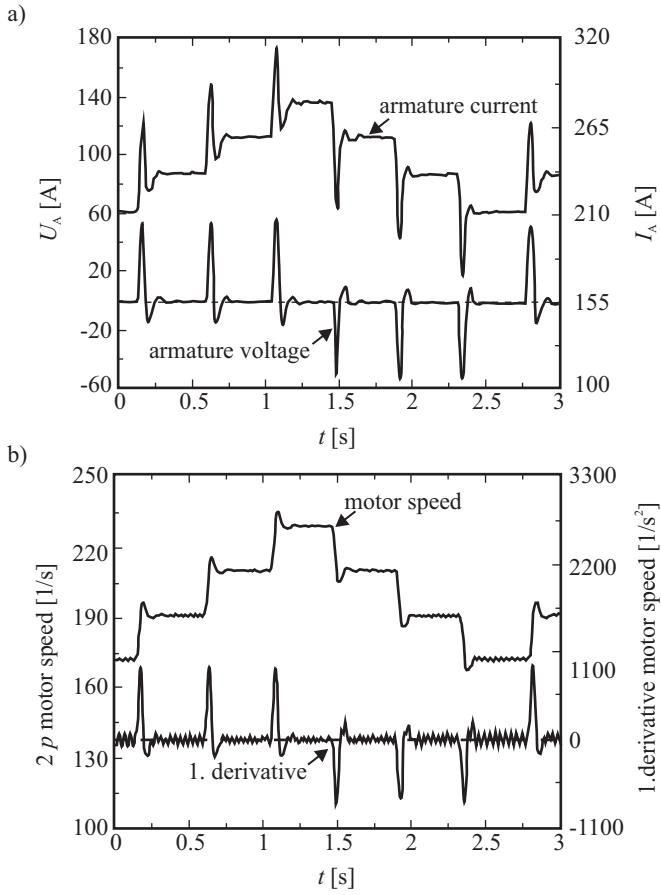


Fig. 24.27. Measured signals for the main drive. **(a)** armature voltage and armature current; **(b)** motor speed ω and first derivative $\dot{\omega}$

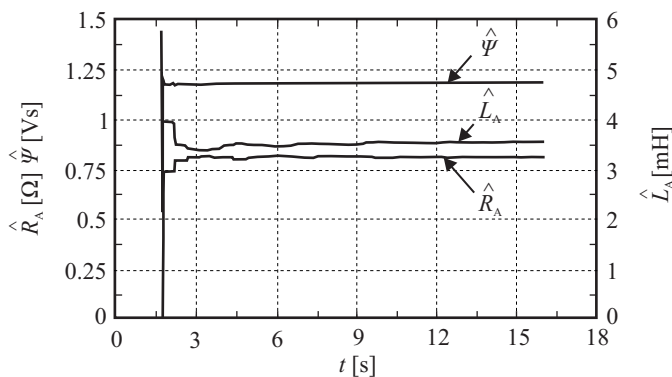


Fig. 24.28. Estimated process coefficients \hat{R}_A , $\hat{\psi}$, and \hat{L}_A of the DC motor

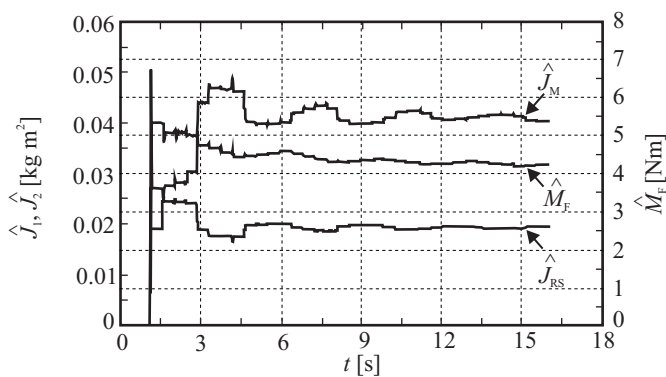


Fig. 24.29. Estimated process coefficients of the main drive. \hat{J}_1 and \hat{J}_2 : moment of inertia of motor and spindle, \hat{M}_C : dry friction torque

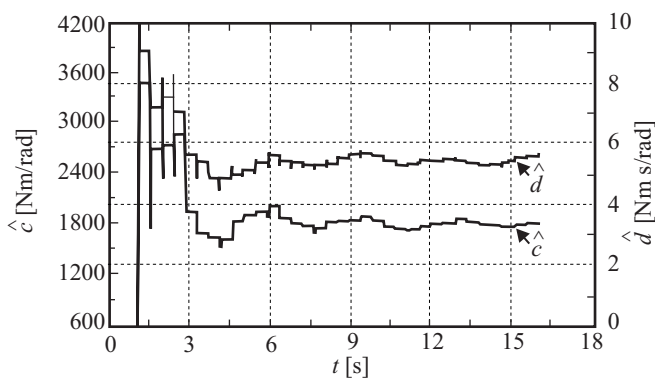


Fig. 24.30. Estimated stiffness \hat{c} and damping \hat{d} of the main drive

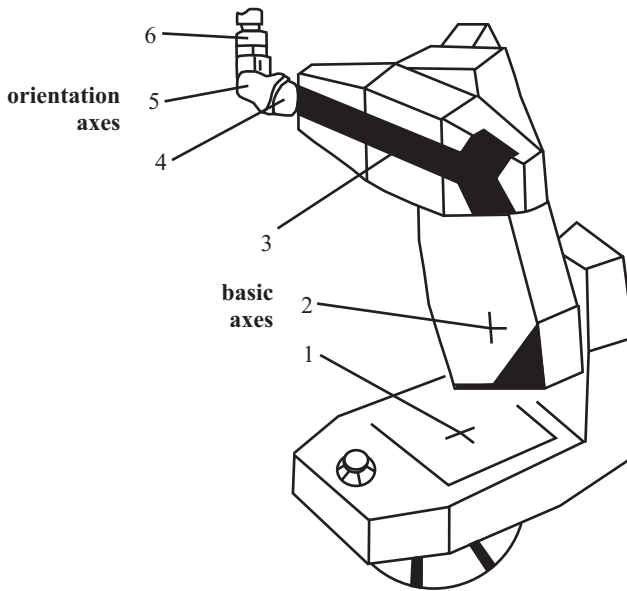


Fig. 24.31. Industrial robot with 6 rotational axes

24.2.2 Industrial Robot

As industrial robots (IR) are usually servo systems with point-to-point movements or trajectory following, they have sufficient dynamic excitation and therefore parameter estimation can be applied very well

Structure of a 6-Axis-Robot

The application of identification methods is in the following described for an industrial robot of type JUNGHEINRICH R106, see Fig. 24.31. The device consists of 6 revolving joints actuated by DC servomotors of high dynamic performance. The following considerations concentrate on the investigation of the mechanical subsystem of the different axes, because a strong demand for parameter estimation techniques exists for applications, such as preventive maintenance and incipient fault diagnosis (Freyermuth, 1991, 1993; Isermann and Freyermuth, 1991).

The mechanical drive chains of the axes consist of different standard machinery elements (gears, bearings, toothed belts, shafts, etc.), transferring torque from the motor to the moved (actuated) arm as shown in Fig. 24.32.

The control of each axis is performed by a cascaded control with an inner speed control of the DC motor and an outer position control of the axis joint. Figure 24.33 depicts the signal flow. The measured variables are the joint position φ , the motor speed ω , and the armature current of the DC motor I_A .

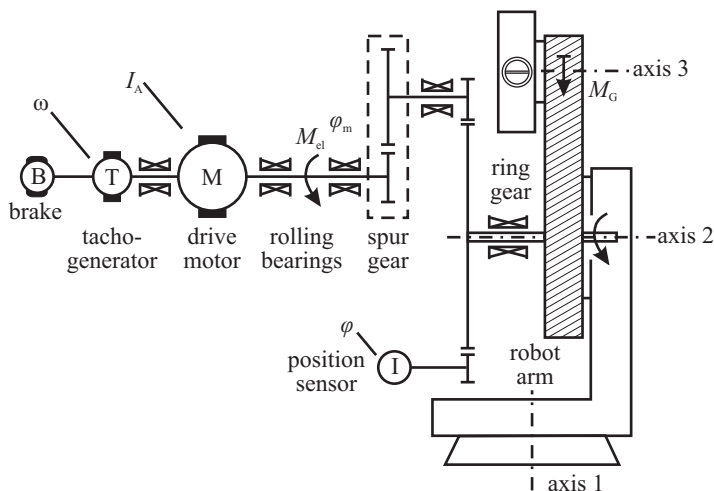


Fig. 24.32. Scheme of the mechanical drive chain (axis) of an industrial robot. Measurable quantities are φ , ω , and I_A

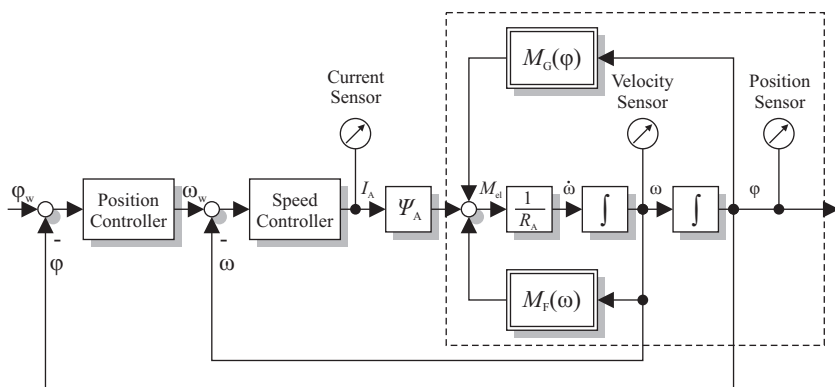


Fig. 24.33. Block diagram of the model of an industrial robot drive unit with conventional cascaded closed control

Assuming the arms as rigid bodies, each joint can be modeled by stating a torque balance related to the joint axis

$$M_{el}(t)/v_i = J_L(\varphi_0, m_L)\ddot{\varphi}(t) + M'_{F0} \text{sign} \dot{\varphi}(t) + M'_{F1} \dot{\varphi}(t) + M'_G(m_L, \varphi_0), \quad (24.2.10)$$

where

$M_{el} = \Psi_A I_A$ electrical torque at motor output axle
 Ψ_A armature flux linkage

I_A	armature current
ν	total gear ratio φ/φ_m
J_L	moment of inertia of the arm (position and load dependent)
M'_{F0}	Coulomb friction torque on joint side
M'_{F1}	viscous friction torque on joint side
M'_G	gravitational torque on joint side
m_L	mass of load at end effector
φ	arm position
φ_0	arm base position
$\omega = \dot{\varphi}/\nu$	motor angular speed

The gravitation torque is modeled by

$$M_G(m_L, \varphi_0) = M'_{G0} \cos \varphi \quad (24.2.11)$$

and may be dependent on a kinematic gravitational torque compensation device, e.g. a pneumatic cylinder. The couplings between the axes can be neglected if the movements are not very fast.

Ψ_A is known from the motor data sheet. Discretizing the continuous-time model (24.2.10) with $k = t/T_0$, T_0 sampling time, and relating the parameters to the motor side by multiplying with ν leads to

$$M_{el}(k) = J(\varphi_0, m_L) \dot{\omega}(k) + M_{F0} \text{sign } \omega(k) + M_{F1} \omega(k) + M_{G0} \cos \varphi(k) \quad (24.2.12)$$

($1/\nu$ is for axis 1, ..., 6: 197, 197, 131, 185, 222, 194)

Then this equation results in vector notation

$$\begin{aligned} M_{el}(k) &= \boldsymbol{\psi}^T(k) \hat{\boldsymbol{\theta}}(k) + e(k) \\ \boldsymbol{\psi}^T(k) &= (\dot{\omega}(k) \text{ sign } \omega(k) \omega(k) \cos \varphi(k)) \\ \hat{\boldsymbol{\theta}} &= \begin{pmatrix} \hat{J} \\ \hat{M}_{F0} \\ \hat{M}_{F1} \\ \hat{M}_{G0} \end{pmatrix} \end{aligned} \quad (24.2.13)$$

and is used for recursive parameter estimation in continuous time with

$$\dot{\omega}(k) = \left. \frac{d\omega(t)}{dt} \right|_k = \frac{\omega(k) - \omega(k-1)}{T_0},$$

where T_0 is a small sampling time. Note that here, the estimated process parameters are identical to the physical defined process coefficients.

Figure 24.34 illustrates the typical behavior of the measured signals in the case of a point-to-point movement (PTP) of basic axis 1. The end effector did not carry any extra load. Sampling interval $T_0 = 5$ ms is identical to that of the position controller for embedding the parameter estimation software into the robot control system. Analog low-pass filtering is realized at a cut-off frequency $f_C = 40$ Hz. Digital filtering to generate the derivative $\dot{\omega}$ is performed at $f_C = 20$ Hz.

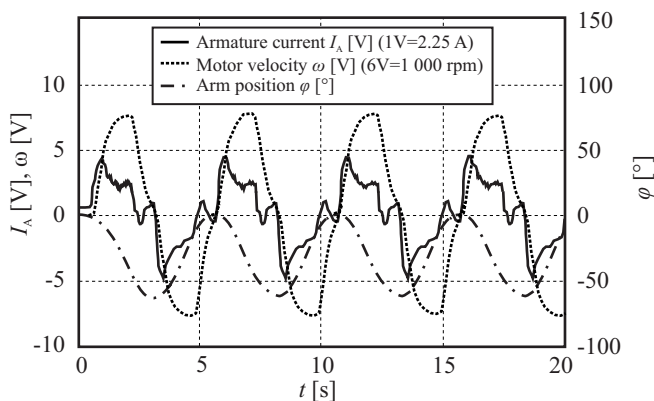


Fig. 24.34. Time history of measurements of basic axis 1 in case of a periodic point-to-point movement

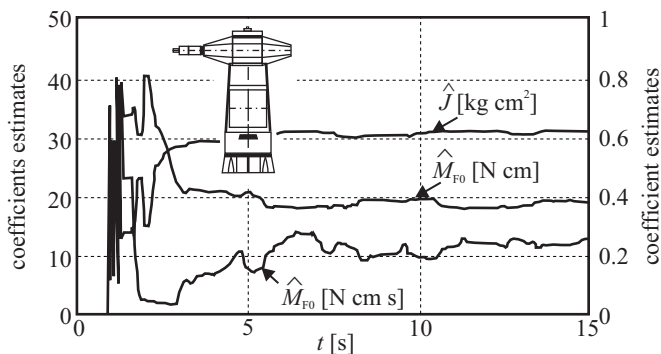


Fig. 24.35. Parameter estimates with the signals of Fig. 24.34

For parameter estimation, the DSFI procedure (discrete square root filtering in information form) is applied, because of its good numerical properties. The forgetting factor λ is set to $\lambda = 0.99$. Figure 24.35 shows the parameter estimates after starting the estimation procedure. They converge within one movement cycle to constant values.

24.2.3 Centrifugal Pumps

Pumps are basic components in most technical processes, like in power and chemical industries, mineral and mining, manufacturing, heating, air conditioning and cooling of engines. They are mostly driven by electrical motors or by combustion engines and consume a high percentage of electrical energy. One distinguishes mainly centrifugal pumps for high deliveries with lower pressures and hydrostatic or positive

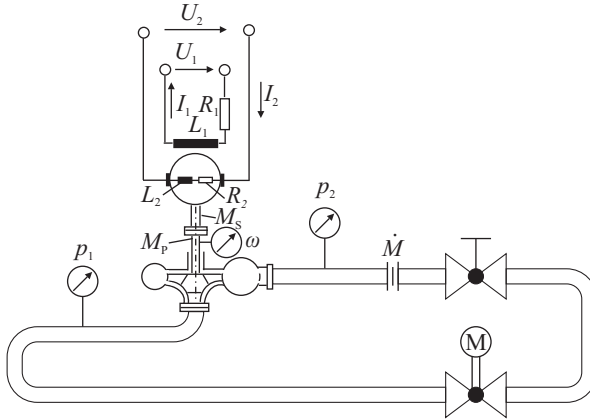


Fig. 24.36. Scheme of the speed-controlled DC motor and centrifugal pump. Closed circuit. Motor: $P_{\max} = 4 \text{ kW}$, $n_{\max} = 3000 \text{ rpm}$, pump: $H = 39 \text{ m}$, $\dot{V}_{\max} = 160 \text{ m}^3/\text{h}$, $n_{\max} = 2600 \text{ rpm}$. An AC motor was used for steady-state operation and a DC motor for dynamic operation.

displacement (reciprocating) pumps for high pressures and small deliveries. They transport pure liquids or mixtures of liquids and solids and herewith increase the pressure to compensate, e.g. for resistance losses or enabling thermodynamic cycles. In the following, this section will concentrate on centrifugal pumps.

In the past, centrifugal pumps were mostly driven with constant speed and the flow rate of liquids was manipulated by valves with corresponding throttling losses. Due to the availability of cheaper speed-controlled induction motors also centrifugal pumps with lower power are now used for directly controlling the flow rate in order to save energy.

The centrifugal pump considered in this example is driven by a speed-controlled DC motor and pumps water through a closed pipe circuit, see Fig. 24.36. Both, the DC motor and the pump are now considered as one unit (Geiger, 1985).

The measured signals are: U_2 armature voltage, I_2 armature current, \dot{V} volume flow rate, ω angular velocity, H pump total head.

The basic equations after some simplifying assumptions are

1. armature circuit

$$L_2 \frac{dI_2(t)}{dt} = -R_2 I_2(t) - \Psi \omega(t) + U_2(t) . \quad (24.2.14)$$

2. mechanics of motor and pump

$$J_P \frac{d\omega}{dt} = \Psi I_2(t) - M_{f0} - \varrho g h_{th1} \omega(t) \dot{V}(t) . \quad (24.2.15)$$

3. hydraulics of the pump (Pfleiderer and Petermann, 2005)

$$H(t) = h_{nn} \omega^2(t) - h_{nv} \omega(t) \dot{V}(t) - h_{vv} \dot{V}^2(t) = h'_{nn} \dot{V}^2(t) . \quad (24.2.16)$$

In this case, all three terms can again be lumped together, as \dot{V} is proportional to ω .

4. hydraulics of the pipe

$$a_F \frac{d\dot{V}(t)}{dt} = -h_{rr} \dot{V}^2(t) + H(t). \quad (24.2.17)$$

The following symbols are used in this example:

L_2	armature inductance	R_2	armature resistance
U_2	armature voltage	I_2	armature current
Ψ	magnetic flux linkage	ω	rotational velocity
J_P	rotational inertia of pump	M_{f0}	dry friction torque
ϱ	density of fluid	g	gravitational constant
h_{th1}	coeff. theoretical pump head	\dot{V}	volume flow rate
H	delivery head	h_{nn}	coefficient of delivery head
h_{nv}	coefficient of delivery head	h_{vv}	coefficient of delivery head
a_F	tube characteristics	h_{rr}	flow friction in tube

The overall model is basically non-linear but linear in the parameters to be estimated. Therefore, least squares parameter estimation can be applied in its direct, explicit form. The models contain 9 process coefficients

$$\mathbf{p}^T = (L_2 \ R_2 \ \Psi \ J_P \ M_{f0} \ h_{th1} \ h'_{nn} \ a_F \ h_{rr}) . \quad (24.2.18)$$

For the parameter estimation, the equations are brought into the form

$$y_j(t) = \boldsymbol{\psi}_j^T(t) \hat{\boldsymbol{\theta}}_j, \quad j = 1, 2, 3, 4, \quad (24.2.19)$$

where

$$\left. \begin{aligned} y_1(t) &= \frac{dI_2(t)}{dt} & y_2(t) &= \frac{d\omega(t)}{dt} \\ y_3(t) &= H(t) & y_4(t) &= \frac{dV(t)}{dt} \end{aligned} \right\} . \quad (24.2.20)$$

The model parameters

$$\hat{\boldsymbol{\theta}}^T = (\hat{\boldsymbol{\theta}}_1^T \ \hat{\boldsymbol{\theta}}_2^T \ \hat{\boldsymbol{\theta}}_3^T \ \hat{\boldsymbol{\theta}}_4^T) \quad (24.2.21)$$

were estimated by the least squares method in the form of discrete square root filtering (DSFI). Based on the model parameter estimates $\hat{\boldsymbol{\theta}}$, all nine process coefficients of \mathbf{p} could be calculated uniquely.

The DC motor is controlled by an AC/DC converter with cascade control of the speed and the armature current as auxiliary control variable. The manipulated variable is the armature current U_2 . A microcomputer DEC-LSI 11/23 was connected online to the process. For the experiments, the reference value $\omega_S(t)$ of the speed control has been changed stepwise with a magnitude of 750 rpm every 2 min. The operating point was $n = 1\,000$ rpm, $H = 5.4$ m, and $\dot{V} = 6.48$ m³/h. The signals were sampled with sampling time $T_0 = 5$ ms and 20 ms over a period of 2.5 s and 10 s, so that 500 samples were obtained. These measurements were stored in the core memory before estimation. Hence, one set of parameters and process coefficients was obtained every 120 s. The results of 550 step changes are shown in Table 24.4.

Table 24.4. Estimated parameters of the pump drive

Parameter	Mean	Std. Dev.
L_2 [mH]	57.6	5.6%
R_2 [Ω]	2.20	5.0%
Ψ [Wb]	0.947	1.2%
J [10^{-3} kg m ²]	24.5	3.7%
c_{R0} [Nm]	0.694	13.5%
h_{TH1} [10^{-3} ms ²]	1.27	3.6%
h_{NN} [10^{-3} ms ²]	0.462	0.8%
a_B [10^3 s ² /m ²]	0.905	1.46%
h_{RR} [10^6 s ² /m ⁵]	1.46	3.9%

24.2.4 Heat Exchangers

Heat exchangers are a typical apparatus in the fields of power and chemical engineering, heating, cooling, refrigeration and air conditioning, and are part of all kind of machines and engines. Their task is to transport heat between two or more media, such as e.g. liquids or gases.

Heat Exchanger Types

A large variety of types exists to meet the specific requirements with regard to temperatures, pressures, phase changes, corrosion, efficiency, weight, space, and connections. Frequently used types are

- tubular heat exchangers
- plate heat exchangers.

With regard to the flow direction, one distinguishes counter flow, parallel flow and cross flow. The fluids are liquids, gases, or steam, resulting in two media with the combinations:

- liquid - liquid
- gas - liquid
- liquid - steam (condensator, evaporator)
- gas - steam

Steam/Water Heat Exchanger

An industrial size steam-heated heat exchanger, see Fig. 24.37, is considered as an example, which is part of a pilot plant (W. Goedecke, 1987; Isermann and Freyermuth, 1991). This plant consists of an electrically powered steam generator, a steam/condensate circulation (circuit 1), a water circulation (circuit 2), and a cross-flow heat exchanger to transport the heat from water to air.

As inputs and outputs of the considered heat exchanger, the following variables are measured:

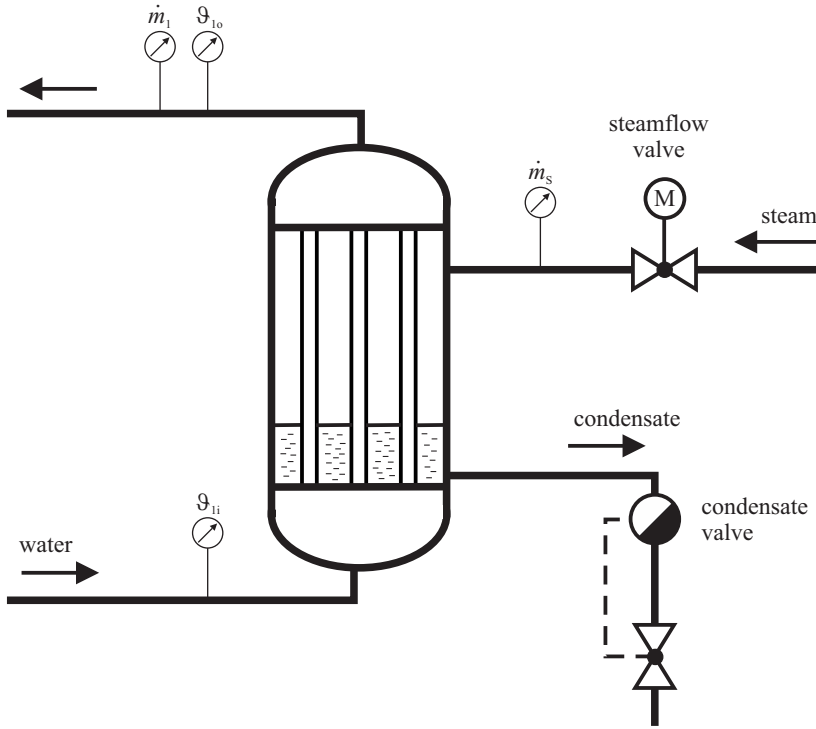


Fig. 24.37. Tubular heat exchanger and measured variables

- \dot{m}_s mass flow of the steam
- \dot{m}_1 mass flow of the liquid fluid (water)
- ϑ_{1i} inlet temperature of the liquid fluid
- ϑ_{1o} outlet temperature of the liquid fluid

The fluid outlet temperature ϑ_{1o} is considered as an output variable, the other three measured variables as input variables.

Linear Models and Parameter Estimation

To model the dynamic behavior, the heat exchanger is subdivided into the tubular section, the water head, a transport delay, and the temperature sensor. The dynamic equations for a heated tube as a distributed parameter process are given e.g. in (Is-ermann, 2010). In addition, balance equations are stated for the steam space and the shell tube. After approximation of the transcendent transfer function with those for lumped parameters and linearization around the operating point, one obtains for example the approximate transfer function

$$\tilde{G}_{s\vartheta}(s) = \frac{\Delta \vartheta_{1o}(s)}{\Delta \dot{m}_s(s)} = \frac{K_s}{(1 + T_{1s}s)(1 + T_{2s}s)} e^{-T_{ds}s} \quad (24.2.22)$$

with

$$\left. \begin{aligned} K_s &= \frac{r}{\dot{m}_1 c_1}, \quad T_{1s} = \frac{1}{v_1} \left(1 + \frac{A_w \varrho_w c_w}{A_1 \varrho_1 c_1} \right) \\ T_{2s} &= \frac{A_w \varrho_w c_w}{\alpha_{w1} U_1} \left(1 + \frac{A_w \varrho_w c_w}{A_1 \varrho_1 c_1} \right) \end{aligned} \right\} \quad (24.2.23)$$

With the quantities being given as

A	area	c_p	specific heat capacity
\dot{m}	mass flow rate	r	vaporization heat
α	heat transfer coefficient	ϑ	temperature
ϱ	density		

and the subscripts

1	primary side of heat exchanger	2	secondary side of heat exchanger
w	wall	s	steam
i	inlet	o	outlet.

In this case, three parameter estimates compare to 10 process coefficients. Therefore, it is not possible to determine all process coefficients uniquely. By assuming some of the process coefficients to be known, however, the following process coefficients and combinations of process coefficients can be determined:

$$\left. \begin{aligned} \alpha_{w1} &= \frac{A_1 \varrho_1 c_1}{T_{2s} U_1} \left(1 - \frac{1}{T_{1s} v_1} \right) \\ A_w \varrho_w c_w &= T_{1s} \dot{m}_1 c_1 - A_1 \varrho_1 c_1 \\ r &= K_s \dot{m}_1 c_1 \end{aligned} \right\} . \quad (24.2.24)$$

The three parameters \hat{K}_s , \hat{T}_{1s} and \hat{T}_{2s} are determined by experiments based on transient function measurements of the fluid outlet temperature ϑ_{1o} due to changes of the input variables ϑ_{1i} , \dot{m}_s and \dot{m}_1 in the direction of decreasing temperature ϑ_{so} . The operating point was

$$\dot{m}_1 = 3000 \frac{\text{kg}}{\text{h}}, \quad \dot{m}_s = 50 \frac{\text{kg}}{\text{h}}, \quad \vartheta_{1i} = 60^\circ\text{C}, \quad \vartheta_{1o} \approx 70^\circ\text{C} .$$

As sampling time, $T_0 = 500$ ms was selected. The time period of one experiment was 360 s, so that 720 samples were taken. For the parameter estimation, the method of total least squares in a recursive form was applied using a digital state variable filter for the determination of the derivatives.

Figure 24.38a shows one measured transient function and Fig. 24.38b the corresponding time history of the parameter estimates. A good convergence of the parameter estimates was obtained in all cases. A verification of the measured and the calculated transient functions shows a very good agreement.

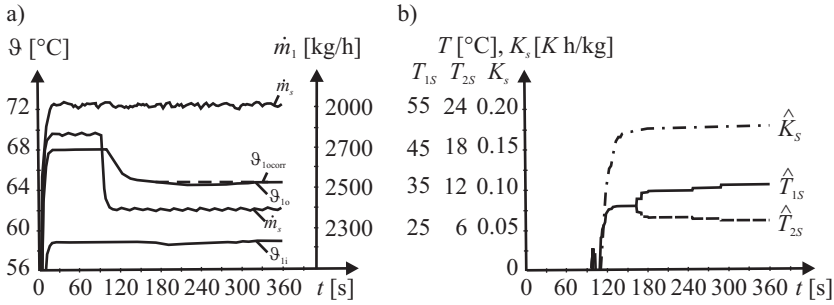


Fig. 24.38. Results for a change in the steam flow $\Delta\dot{m}_s$: (a) Measured transient functions for a steam flow change, (b) parameter estimates from transient function

Parameter Variable Local Linear Models

As the behavior of heat exchangers depends strongly on the flow-rates, the static and dynamic behavior is non-linear for changing flow-rates. In order to develop models which are applicable over a large operating range, local linear neuronal netmodels of the type LOLIMOT were used to describe first the nominal behavior. This was applied to the steam/water heat exchanger used also for Sect. 24.2.4. By using the LOLIMOT identification method, dynamic models of the water outlet temperature ϑ_{10} in dependence on the water volume flow \dot{V}_1 , steam mass flow \dot{m}_s , and inlet temperature ϑ_{1i} were determined by simultaneous wide range excitation of the two flows with amplitude modulated PRBS signals (Ballé, 1998).

This resulted in 10 local linear models in dependence on the water flow. Using a sample time of $T_0 = 1$ s, a second order dynamic model was sufficient

$$\begin{aligned} \vartheta_{10}(k) = & -a_1(z)\vartheta_{10}(k-1) - a_2(z)\vartheta_{10}(k-1) \\ & + b_{11}(z)\dot{m}_s(k-1) + b_{12}(z)\dot{m}_s(k-2) \\ & + b_{21}(z)\dot{V}_1(k-1) + b_{31}(z)\vartheta_{1i}(k-1) + c_0(z), \end{aligned} \quad (24.2.25)$$

where the parameters depend on the operating point $z = \dot{V}_1$

$$a_v(\dot{V}_1) = \sum_{j=1}^{10} a_v \Phi_j(\dot{V}), \quad b_{v\mu}(\dot{V}_1) = \sum_{j=1}^{10} b_{v\mu}(\dot{V}), \quad c_0(\dot{V}_1) = \sum_{j=1}^{10} c_0 \Phi_j(\dot{V}), \quad (24.2.26)$$

where Φ_j is the weighting function within LOLIMOT.

Figure 24.39 shows the resulting stationary outlet temperature in dependence on the two flows. The identified models then allowed to extract three gains and one dominant time constant, partially depicted in Fig. 24.40. The operating point dependence is especially strong for low water flow rates. Static gains and the time constant change with about a factor four.

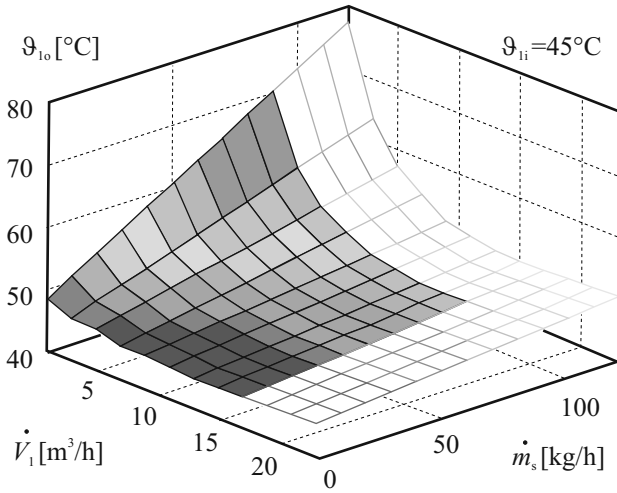


Fig. 24.39. Heat exchanger water outlet temperature static map in dependence on water and steam flow

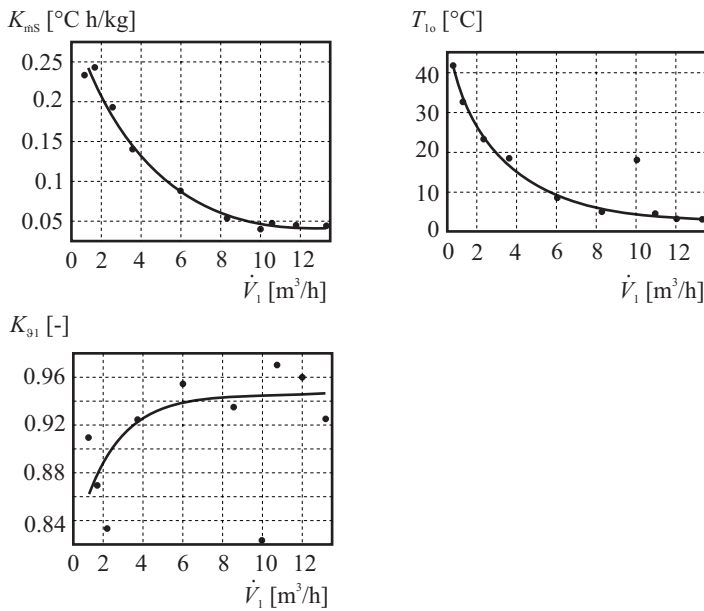


Fig. 24.40. Static gains and time constant for the water outlet temperature in dependence on the water flow rate

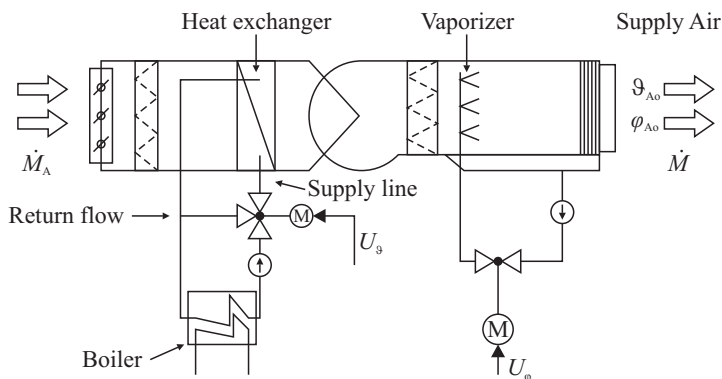


Fig. 24.41. Schematic view of an air condition unit (air mass flow $\dot{M}_{A,\max} = 500 \text{ m}^3/\text{s}$)

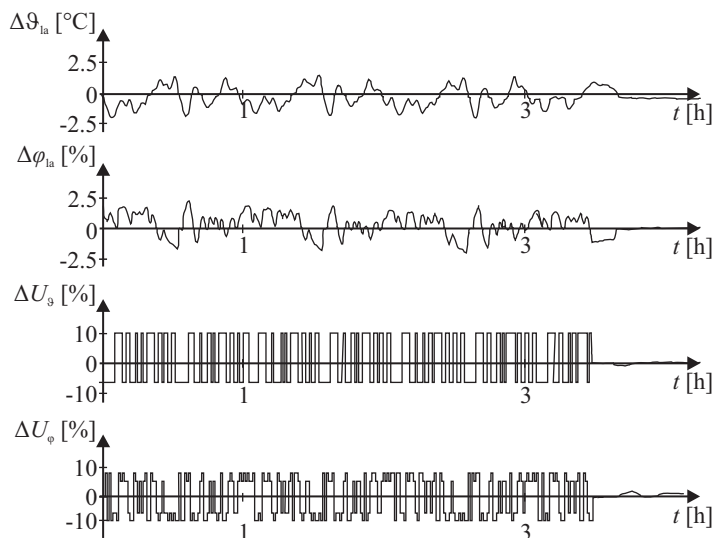


Fig. 24.42. Measurements at an air condition unit. Operating point: $\vartheta_{A0} = 30^\circ\text{C}$, $\varphi_{A0} = 35^\circ\text{C}$, $T_0 = 1 \text{ min}$. Test signal amplitudes: $u_1 = 1 \text{ V}$ and $u_2 = 0.8 \text{ V}$

24.2.5 Air Conditioning

The air condition system that is considered in this section consists of a heater and a humidifier, see Fig. 24.41. By means of the hot water supply, the air temperature after the cross-flow heat exchanger is controlled. Inside the humidifier, the humidity is controlled by means of the water spray flow. Figure 24.42 shows the measurements that have been taken at the process. Since it was a linear MIMO process, a PRBS for the first input was combined with an orthogonal PRMS in order not to apply corre-

lated input signals. The clock time of the base PRBS was $\lambda = 1$, the measurement time was $T_M = 195$ s. As a model structure, a simplified P-canonical model was chosen. The model order and dead time estimation by employing a determinant test provided $\hat{m}_1 = 2$, $\hat{d}_{11} = 0$, $\hat{d}_{12} = 0$, and $\hat{m} = 1$, $\hat{d}_{21} = 0$, $\hat{d}_{22} = 0$. By means of COR-LS, the following models (Hensel, 1987) were then identified

$$\begin{aligned}\hat{G}_{11}(z) &= \frac{\Delta \vartheta_{Ao}}{\Delta U_{\vartheta}(z)} = \frac{0.0509z^{-1} + 0.0603z^{-2}}{1 - 0.8333z^{-1} + 0.1493z^{-2}} \\ \hat{G}_{21}(z) &= \frac{\Delta \vartheta_{Ao}}{\Delta U_{\varphi}(z)} = \frac{-0.0672z^{-1} - 0.0136z^{-2}}{1 - 0.8333z^{-1} + 0.1493z^{-2}} \\ \hat{G}_{22}(z) &= \frac{\Delta \varphi_{Ao}}{\Delta U_{\varphi}(z)} = \frac{0.2319z^{-1}}{1 - 0.3069z^{-1}} \\ \hat{G}_{11}(z) &= \frac{\Delta \vartheta_{Ao}}{\Delta U_{\vartheta}(z)} = \frac{0.0107z^{-1}}{1 - 0.3069z^{-1}}.\end{aligned}$$

The estimated static gains result as $\hat{K}_{11} = 0.3520$, $\hat{K}_{12} = -0.2557$, $\hat{K}_{22} = 0.3345$, and $\hat{K}_{12} = 0.0154$. The coupling from $\Delta U_{\vartheta}(z)$ to $\Delta \varphi_{Ao}(z)$ is hence negligible.

24.2.6 Rotary Dryer

A rotary dryer for sugar beets has been identified as described in (Mann, 1980) and (Isermann, 1987). The input to the process is the amount of fuel supplied, \dot{m}_F , and the output is the amount of dry matter, ψ_{DM} . The process shows large disturbances, hence the identification results that had been obtained in the short measurement time are not optimal. Figure 24.43 however shows that the measured output and model output match quite well for longer identification times of roughly 6 hours. The difference in the DC values can be explained by the large disturbances. The process model, which was identified using COR-LS, is given as

$$G(z) = \frac{-1.15z^{-1} + 1.52z^{-2} - 0.54z^{-3} + 0.27z^{-4} + 0.27z^{-5}}{1 - 2.01z^{-1} + 1.27z^{-2} - 0.24z^{-3} + 0.07z^{-4} - 0.07z^{-5}} z^{-2}, \quad (24.2.27)$$

see also Fig. 24.45. One can see from the calculated step response in Fig. 24.44 that the resulting model has an all-pass behavior and contains a dead time.

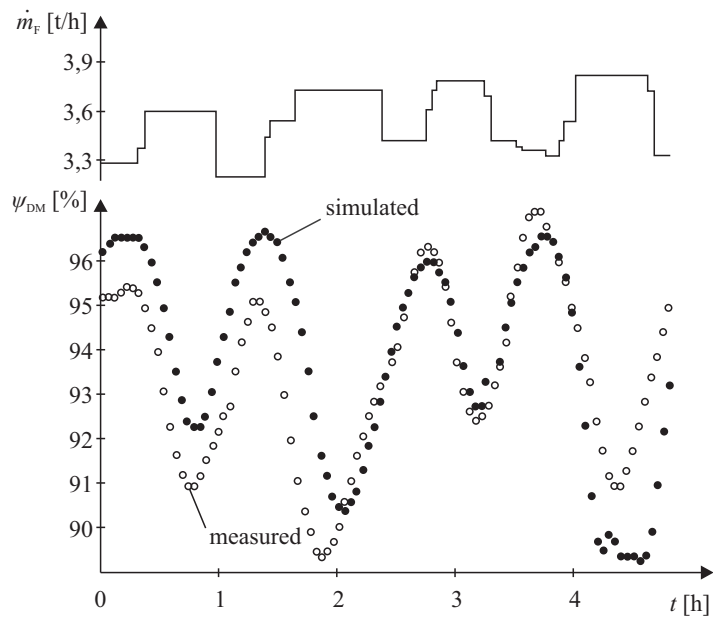


Fig. 24.43. Signals for the identification of a rotary dryer

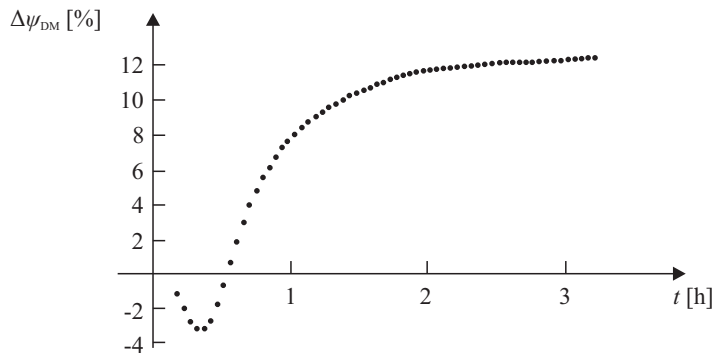


Fig. 24.44. Step response for a change in the manipulated variable fuel mass of the rotary dryer calculated from the identified model

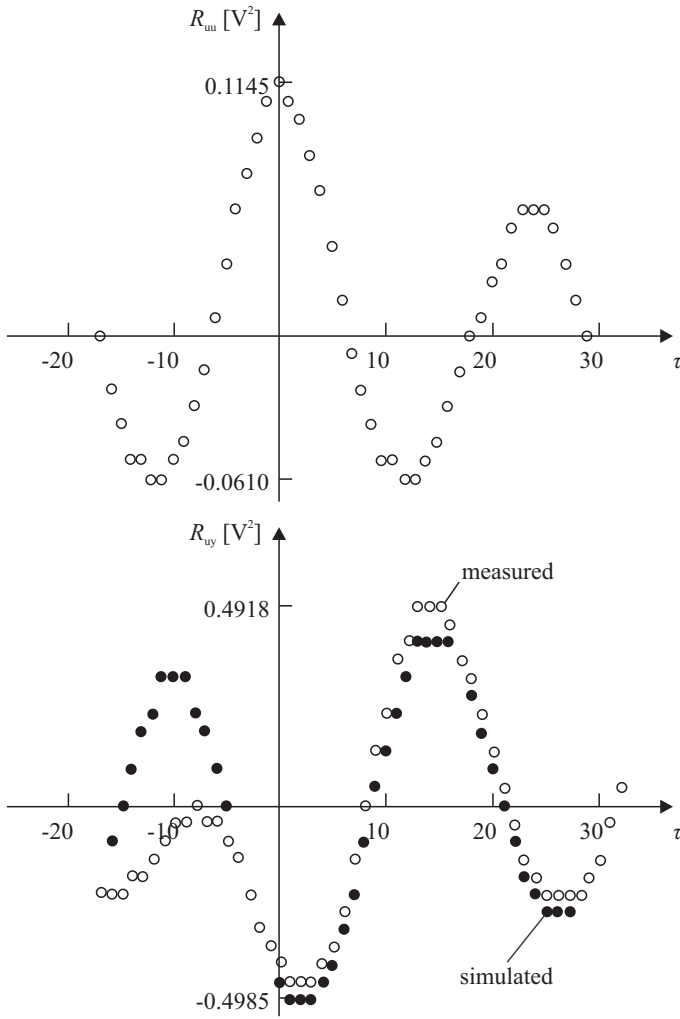


Fig. 24.45. Auto-correlation and cross-correlation function of the rotary dryer

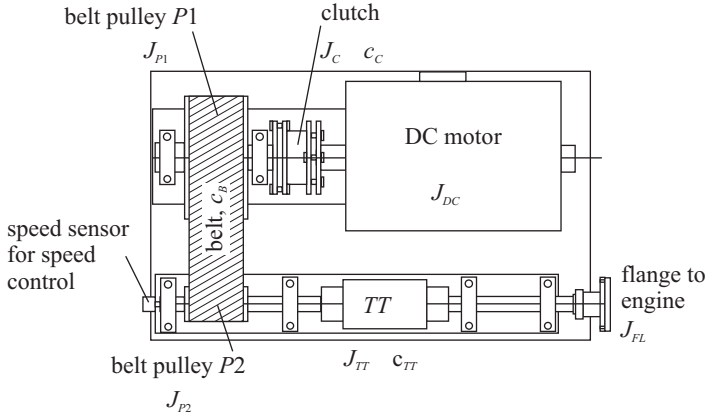


Fig. 24.46. Arrangement of the engine test stand

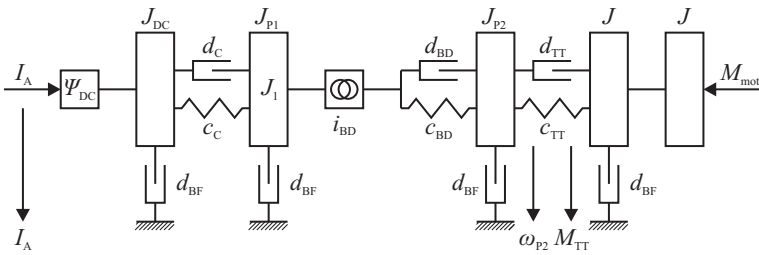


Fig. 24.47. Schematic of the rotational dynamics of the engine test stand

24.2.7 Engine Teststand

Dynamic models of a combustion engine testbench are required for designing the torque or speed control. Figure 24.46 shows the setup. The testbed consists of a DC motor, a spring shackle clutch, a belt transmission, a torque transducer, and a flange to connect the combustion engine to the testbed. The dynamometer applies a dynamic load torque to the combustion engine, which can be shaped to correspond to a certain driving cycle. To design a suitable controller, a precise linear model of the dynamics was required. The input signal of the process is the armature current of the DC motor I_A , the output is the torque at the torque transducer M_{TT} (Voigt, 1991; Pfeiffer, 1997).

Figure 24.47 shows a schematic diagram of the engine testbench with five rotational inertias, which are coupled by spring/damper combinations. The friction in the roller bearings is modeled as viscous friction. The linear behavior can be described by a linear state space model as

$$\dot{\mathbf{x}}(t) = \mathbf{A}\mathbf{x}(t) + \mathbf{b}u(t) + \mathbf{g}n(t) \quad (24.2.28)$$

$$\mathbf{y}(t) = \mathbf{C}\mathbf{x}(t) \quad (24.2.29)$$

with the input $u(t)$ being the armature current $I_A(t)$, the disturbance $n(t)$ being the torque exerted by the engine $M_{\text{mot}}(t)$, and

$$\mathbf{x}(t)^T = (\omega_{\text{FL}} \Delta\varphi_{\text{TT}}(t) \omega_{\text{P2}}(t) \Delta\varphi_{\text{BD}}(t) \omega_{\text{P1}}(t) \Delta\varphi_{\text{C}}(t) \omega_{\text{DC}}(t)) \quad (24.2.30)$$

$$\mathbf{y}(t) = (M_{\text{TT}}(t) \omega_{\text{P2}}(t)) . \quad (24.2.31)$$

The model parameters are given as

$$\mathbf{A} = \begin{pmatrix} -\frac{d_{\text{TT}}+d_{\text{BF}}}{J_{\text{FL}}+J_{\text{mot}}} & \frac{c_{\text{TT}}}{J_{\text{FL}}+J_{\text{mot}}} & \frac{d_{\text{TT}}}{J_{\text{FL}}+J_{\text{mot}}} & 0 & 0 & 0 & 0 \\ -1 & 0 & 1 & 0 & 0 & 0 & 0 \\ \frac{d_{\text{TT}}}{J_{\text{P2}}} & -\frac{c_{\text{TT}}}{J_{\text{P2}}} & -\frac{d_{\text{BD}}+d_{\text{TT}}+d_{\text{BF}}}{J_{\text{P2}}} & \frac{c_{\text{BD}}}{J_{\text{P2}}} & \frac{i_{\text{BD}}d_{\text{BD}}}{J_{\text{P2}}} & 0 & 0 \\ 0 & 0 & -1 & 0 & i_{\text{BD}} & 0 & 0 \\ 0 & 0 & \frac{i_{\text{BD}}d_{\text{BD}}}{J_{\text{P1}}} & -\frac{i_{\text{BD}}c_{\text{BD}}}{J_{\text{P1}}} & \frac{i_{\text{BD}}^2d_{\text{BD}}+d_{\text{C}}+d_{\text{BF}}}{J_{\text{P1}}} & \frac{c_{\text{C}}}{J_{\text{P1}}} & \frac{d_{\text{C}}}{J_{\text{P1}}} \\ 0 & 0 & 0 & 0 & -1 & 0 & 1 \\ 0 & 0 & 0 & 0 & \frac{d_{\text{C}}}{J_{\text{DC}}} & -\frac{c_{\text{C}}}{J_{\text{DC}}} & \frac{d_{\text{C}}+d_{\text{BF}}}{J_{\text{DC}}} \end{pmatrix} \quad (24.2.32)$$

$$\mathbf{b}^T = \left(0 \ 0 \ 0 \ 0 \ 0 \ 0 \ \frac{\Psi_{\text{DC}}}{J_{\text{DC}}} \right) \quad (24.2.33)$$

$$\mathbf{C} = \begin{pmatrix} 0 & c_{\text{TT}} & 0 & 0 & 0 & 0 & 0 \\ 0 & 0 & 1 & 0 & 0 & 0 & 0 \end{pmatrix} . \quad (24.2.34)$$

The transfer function matrix can then be determined by

$$\mathbf{G}(s) = \mathbf{C}(s\mathbf{I} - \mathbf{A})^{-1}\mathbf{b} . \quad (24.2.35)$$

Considering $I_A(t)$ as an input and $M_{\text{TT}}(t)$ as an output, the model is of seventh order

$$G_{\text{IT}}(s) = \frac{b_0 + b_1s}{a_0 + a_1s + a_2s^2 + a_3s^3 + a_4s^4 + a_5s^5 + a_6s^6 + a_7s^7} . \quad (24.2.36)$$

The parameters of the transfer function depend on the physical parameters of the system. Here, the quantities are given as

Ψ_{DC}	magnetic flux linkage DC	J	rotational moment of inertia
c	spring stiffness	d	damping coefficient
ω	rotational velocity	φ	angle
M	torque	I	current

and the indices denote

BF	bearing friction	P2	belt pulley P2
DC	DC motor	TT	torque transducer
C	clutch	FL	flange
P1	belt pulley P1	mot	test engine
BD	belt drive.		

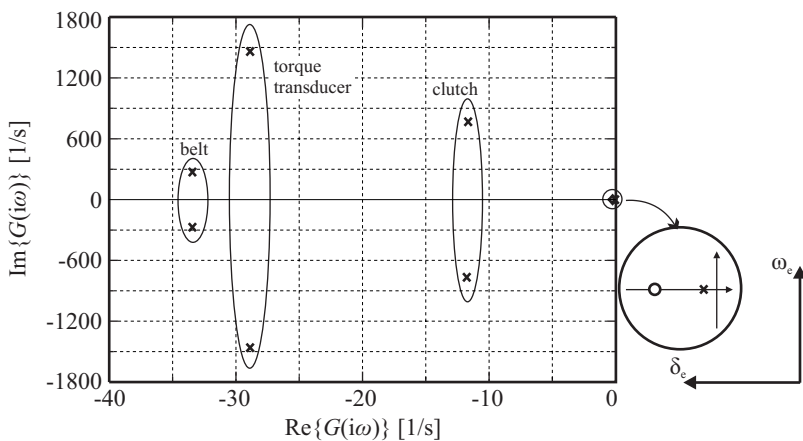


Fig. 24.48. Poles and zeros of the transfer function of the engine test stand

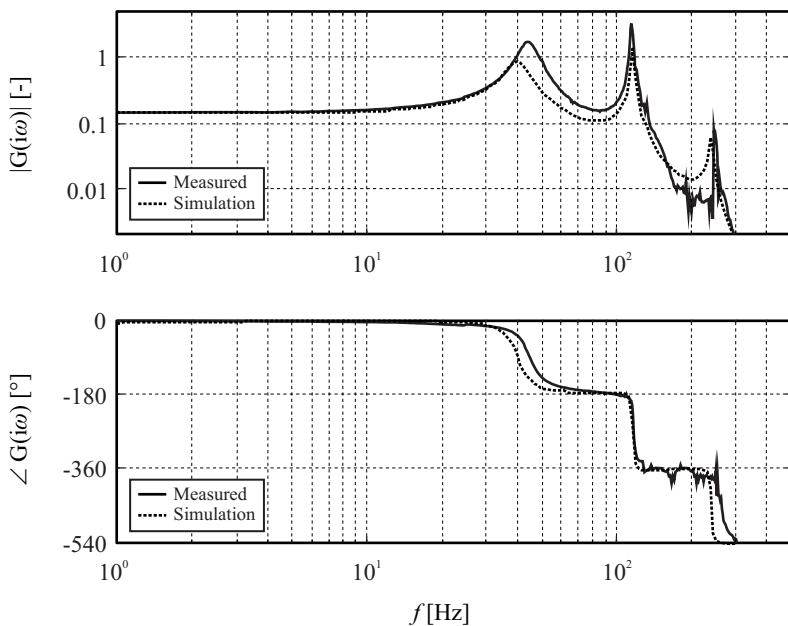


Fig. 24.49. Measured frequency response of the mechanical part of the test stand for current $I_A(t)$ as input and the torque $M_{TT}(t)$ as output

Figure 24.48 shows the poles and zeros of the transfer function. Three pairs of conjugate complex poles are obtained, as well as one real pole and one real zero. Hence, the following natural angular eigenfrequencies can be distinguished $\omega_{e,C}$ for the clutch, $\omega_{e,TT}$ for the torque transducer, and $\omega_{e,B}$ for the belt. Considering the not-coupled elements as undamped second order systems, the characteristic frequencies can be determined as

$$f_{0,C} = \frac{1}{2\pi} \sqrt{\frac{c_C(J_{DC} + J_{P1})}{J_{DC}J_{P1}}} = 154.7 \text{ Hz (clutch)} \quad (24.2.37)$$

$$f_{0,BD} = \frac{1}{2\pi} \sqrt{\frac{c_{BD}(J_{DC} + J_{P1}) + i_{BD}^2(J_{P2} + J_{FL})}{(J_{DC}J_{P1})(J_{P2} + J_{FL})}} = 34.5 \text{ Hz (belt)} \quad (24.2.38)$$

$$f_{0,TT} = \frac{1}{2\pi} \sqrt{\frac{c_{TT}(J_{P2} + J_{FL})}{J_{P2}J_{FL}}} = 154.7 \text{ Hz (clutch)} \quad (24.2.39)$$

Figure 24.49 shows the measured frequency response of the system without an engine attached. The three resonance frequencies of the belt (approximately 45 Hz), clutch (120 Hz), and torque transducer (250 Hz) can clearly be recognized. The results show a good agreement between model and measurement (Isermann et al, 1992; Pfeiffer, 1997). The obtained model allowed the design of a digital torque controller with the connected combustion engine, allowing the compensation of the testbed dynamics with accurate powertrain models up to frequencies of 12 Hz.

24.3 Automotive Vehicles

Automotive vehicles are another interesting area of application, where the use of experimental modeling is of great benefit. While the vehicle dynamics can very well be modeled by a one-track or a two-track model, it is very hard to derive the model parameters analytically. Furthermore, many parameters, describing e.g. the mass distribution and the wheel-road-friction, vary over time as e.g. the load changes or the road surface is dry or wet or icy depending on the weather. Therefore, advanced vehicle dynamics systems have to be adapted to the varying parameters of the vehicle.

Further examples presented in this section include the estimation of wheel suspension system and tire parameters. Both of these are safety critical systems and hence knowledge about the state of these components is of great benefit in terms of supervision of these components. Another safety critical system is the braking system, which will also be modeled and identified in this section.

Finally, combustion engines will be treated. With more and more strict emission requirements, the amount of actuators at the combustion engine increases steadily, making these system true (nonlinear) MIMO systems.

24.3.1 Estimation of Vehicle Parameters

In this section, the estimation of vehicle parameters shall be described. The estimation of vehicle parameters is of interest for advanced vehicle dynamic control

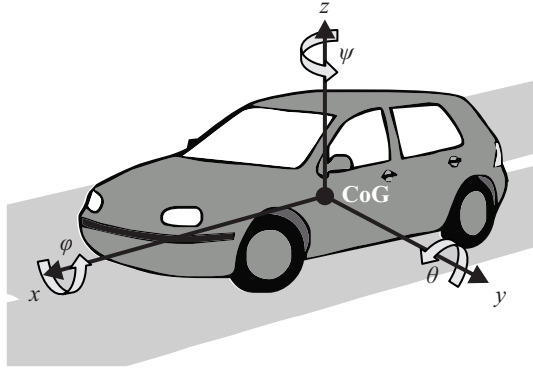


Fig. 24.50. Coordinate system of a road vehicle (Halbe, 2008; Schorn, 2007)

systems, which can employ such an automatically adapted model for model-based control algorithms.

A simple yet sufficiently precise model is the one-track model, (Milliken and Milliken, 1997), which can describe the dynamic behavior of a car up to lateral accelerations of roughly $a_Y \leq 0.4g$. For the one-track model, in contrast to the two-track model, both wheels of each axle are combined into a single wheel at the center of the axle. Furthermore, it is assumed that the center of gravity of the car is on the road surface, i.e. the car does not roll. The force buildup between the tire surface and the road is also assumed to be linearly dependent on the slip angle. Due to these simplifying assumptions, the one-track model is not always of sufficient fidelity, but it can be used in most situations that a normal driver experiences.

Figure 24.50 shows the coordinate system of a passenger car and shall be used to explain the symbols that will be used in the following: x , y , and z describe the three lateral degree of freedom of the car, whereas ϕ denotes the roll, ψ denotes the yaw, and θ denotes the pitch angle.

The characteristics of a tire governing the tire-road surface interaction are shown in Fig. 24.51. Here, one can see that the cornering friction force depends non-linearly on the slip angle, but for small side slip angles can be assumed to be a linear function of the side slip angle.

The one-track model, see Fig. 24.52, can now be derived based on the force and momentum balance of the vehicle,

$$\underbrace{m \frac{v^2}{R} \sin \beta - m \dot{v} \cos \beta}_{\text{D'Alembert inertial forces}} + \underbrace{F_{x\text{r}} + F_{x\text{f}} \cos \delta - F_{y\text{f}} \sin \delta}_{\text{tire forces}} = 0 \quad (24.3.1)$$

$$\underbrace{-m \frac{v^2}{R} \cos \beta - m \dot{v} \sin \beta}_{\text{D'Alembert inertial forces}} + \underbrace{F_{y\text{r}} + F_{x\text{f}} \sin \delta - F_{y\text{f}} \cos \delta}_{\text{tire forces}} = 0 \quad (24.3.2)$$

$$-J_z \ddot{\psi} + (F_{y\text{f}} \cos \delta + F_{x\text{f}} \sin \delta) l_{\text{f}} - F_{y\text{h}} l_{\text{h}} = 0. \quad (24.3.3)$$

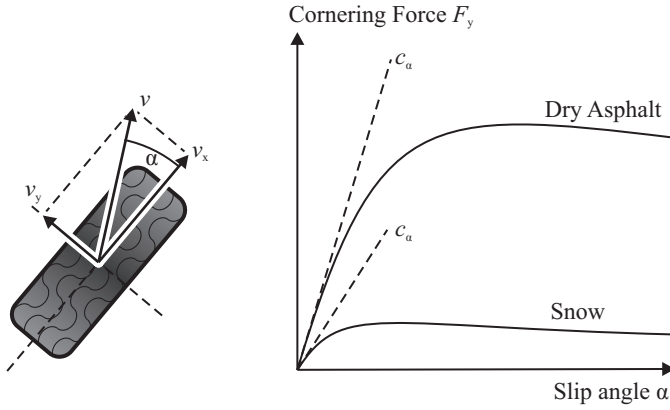


Fig. 24.51. Definition of slip angle and tire characteristics (Halbe, 2008; Schorn, 2007)

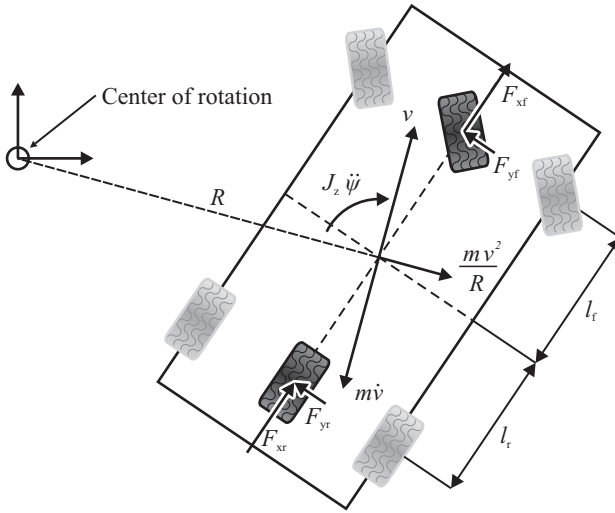


Fig. 24.52. Schematic of the one-track model of a vehicle (Halbe, 2008; Schorn, 2007)

Also, one has the following kinematic relations:

$$\alpha_r = \arctan\left(\frac{v_{yr}}{v_{xr}}\right) = \arctan\left(\frac{l_r \dot{\psi} - v \sin \beta}{v \cos \beta}\right) \approx \left(\frac{l_r \dot{\psi} - v \sin \beta}{v \cos \beta}\right) \quad (24.3.4)$$

$$\alpha_f = \delta - \arctan\left(\frac{l_f \dot{\psi} + v \sin \beta}{v \cos \beta}\right) \approx \delta - \left(\frac{l_f \dot{\psi} + v \sin \beta}{v \cos \beta}\right), \quad (24.3.5)$$

which provide the slip angle of the front and rear wheel. From there, one can determine the lateral tire forces as

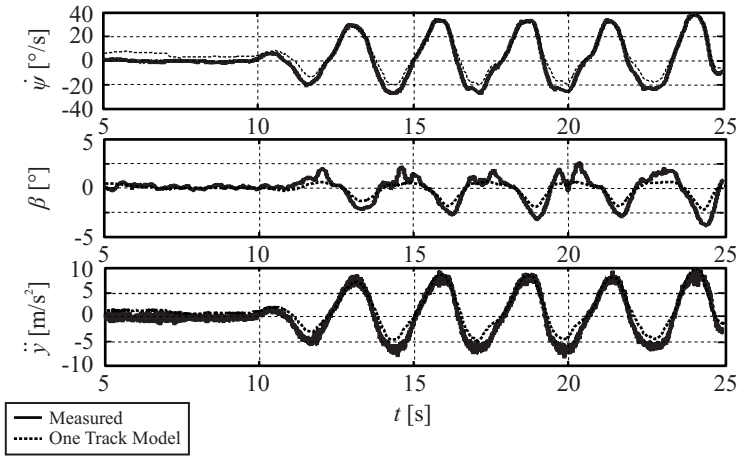


Fig. 24.53. Driving maneuver with a parameterized single track model (Halbe, 2008; Schorn, 2007)

$$f_{yr} = c_{\alpha r} \alpha_r \quad (24.3.6)$$

$$f_{yf} = c_{\alpha f} \alpha_f . \quad (24.3.7)$$

Finally, the one track model can be written in state space form as

$$\begin{pmatrix} \ddot{\psi} \\ \ddot{\beta} \end{pmatrix} = \begin{pmatrix} \frac{-c_{\alpha f} l_f^2 + c_{\alpha r} l_r^2}{m v^2} & \frac{-c_{\alpha f} l_f + c_{\alpha r} l_r}{m v} \\ \frac{J_z v}{m v^2} & \frac{J_z}{m v} + c_{\alpha r} \end{pmatrix} \begin{pmatrix} \dot{\psi} \\ \dot{\beta} \end{pmatrix} + \begin{pmatrix} \frac{c_{\alpha f} l_f + c_{\alpha r} l_r}{m v} \\ \frac{J_z i_s}{m v i_s} \end{pmatrix} \delta_H . \quad (24.3.8)$$

In these equations, the following symbols are used:

m	mass	v	velocity
R	instantaneous radius	β	slip angle
δ	steering angle	J	moment of inertia
l	length	α	side slip angle
c_α	cornering stiffness		

with the indices

fl	front left	fr	front right
rl	rear left	rr	rear right.

One can now use test drives to estimate the parameters of the one track model. The results for a one track model that has been parameterized by a test drive is shown in Fig. 24.53, where one can see the good match between the model output and the measurement. For more details see (Wesemeier and Isermann, 2007; Halbe, 2008; Schorn, 2007).

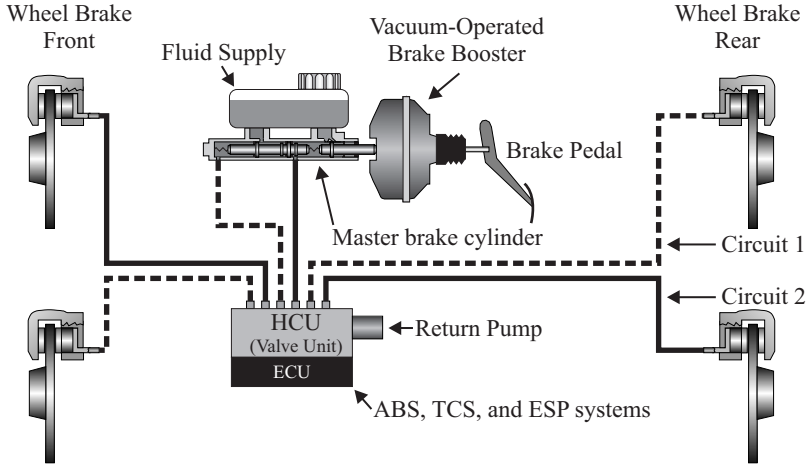


Fig. 24.54. Schematic of a hydraulic vehicle braking system

24.3.2 Braking Systems

This section is concerned with the modeling and identification of components of a hydraulic passenger car braking systems. A schematic view of such a system is shown in Fig. 24.54. The foot force exerted by the driver is amplified by means of a vacuum operated brake booster and is then transmitted to the master brake cylinder, which is typically mounted directly at the vacuum brake booster. The master brake cylinder is divided into two separate chambers by the intermediate piston. From the master brake cylinder, two separate lines run to the hydraulic control unit, which houses all valves for the anti-lock braking system, the traction control system, etc. Four lines connect this block to the four wheel brake cylinders. In the wheel brake cylinders, brake pads can be pushed against the brake disk in order to generate a friction torque which in turn will slow the vehicle down. More detailed information can be found in (Robert Bosch GmbH, 2007; Burckhardt, 1991; Breuer and Bill, 2006).

Hydraulic subsystem

In the following, a detailed model of the hydraulic subsystem of the braking system used at a passenger car braking system testbed (Fig. 24.55) will be derived. This model will be formulated as a non-linear state-space model, with the dynamics of the system being governed by the set of first order non-linear differential equations,

$$\dot{x} = a(x) + Bu \quad (24.3.9)$$

and the output given as

$$y = c^T x + d^T u. \quad (24.3.10)$$

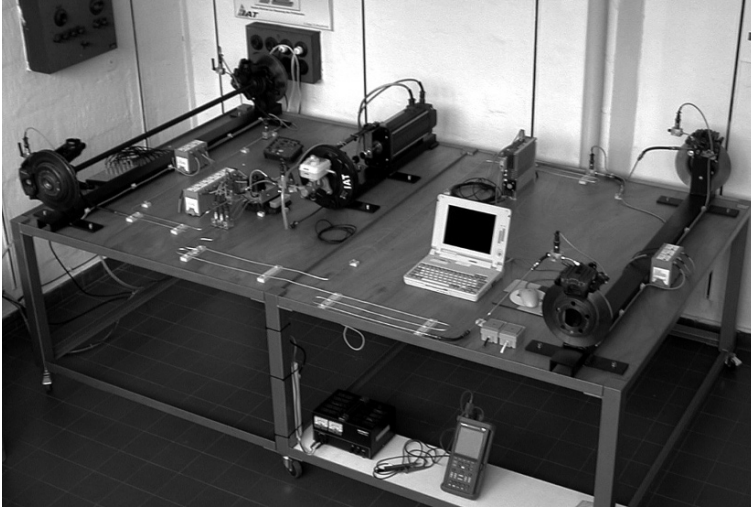


Fig. 24.55. View of the braking system testbed at IAT, TU Darmstadt (Straky, 2003)

Here and in the remainder of this section, the following symbols are used:

V	volume
\dot{V}	volume flow rate
R_T	turbulent flow resistance
R_L	laminar flow resistance
L	inertia of hydraulic fluid
C	capacity of wheel brake cylinder chamber
p	pressure

and the indices denote

fl	front left
fr	front right
rl	rear left
rr	rear right
I	chamber 1 of master brake cylinder
II	chamber 2 of master brake cylinder
wbc	wheel brake cylinder

Upon operation of the brake pedal, the master brake cylinder will push a certain amount of brake fluid into the individual wheel brake cylinders. This amount of fluid displaced along with the time rate of change of this displacement will be chosen as the states of the system,

$$\mathbf{x} = (V_{fl} \dot{V}_{fl} V_{fr} \dot{V}_{fr} V_{rl} \dot{V}_{rl} V_{rr} \dot{V}_{rr})^T. \quad (24.3.11)$$

If subjected to a pressure, the master brake cylinder and the hydraulic connection lines will widen and the hydraulic fluid will be compressed, all of which will lead to a

consumption of brake fluid. The flow through the valves inside the hydraulic control unit will give rise to turbulent flow losses. Some of the valves are backflow valves, hence the pressure loss depends on the flow direction and must hence be modeled flow-direction dependent. The long connection lines evoke laminar flow losses. The wheel brake cylinders are modeled as compressible volumes. This once again captures the widening of the cylinder walls and the caliper as well as the compression of the brake pads, brake discs and brake fluid due to a pressure increase.

The dynamics of the system are then governed by

$$a(\mathbf{x}) = \begin{pmatrix} \dot{V}_{fl} \\ -\frac{R_{T,fl}}{L_{fl}} \dot{V}_{fl}^2 - \frac{R_{L,fl}}{L_{fl}} \dot{V}_{fl} - \frac{1}{L_{fl}} \int \frac{\dot{V}_{fl}}{C_{fl}(V_{fl})} dt \\ \dot{V}_{fr} \\ -\frac{R_{T,fr}}{L_{fr}} \dot{V}_{fr}^2 - \frac{R_{L,fr}}{L_{fr}} \dot{V}_{fr} - \frac{1}{L_{fr}} \int \frac{\dot{V}_{fr}}{C_{fr}(V_{fr})} dt \\ \dot{V}_{rl} \\ -\frac{R_{T,rl}}{L_{rl}} \dot{V}_{rl}^2 - \frac{R_{L,rl}}{L_{rl}} \dot{V}_{rl} - \frac{1}{L_{rl}} \int \frac{\dot{V}_{rl}}{C_{rl}(V_{rl})} dt \\ \dot{V}_{rr} \\ -\frac{R_{T,rr}}{L_{rr}} \dot{V}_{rr}^2 - \frac{R_{L,rr}}{L_{rr}} \dot{V}_{rr} - \frac{1}{L_{rr}} \int \frac{\dot{V}_{rr}}{C_{rr}(V_{rr})} dt \end{pmatrix}. \quad (24.3.12)$$

This input distribution matrix \mathbf{B} is defined as

$$\mathbf{B} = \begin{pmatrix} 0 & 0 & 0 & \frac{1}{L_{fl}} & 0 & \frac{1}{L_{rl}} & 0 & 0 \\ 0 & \frac{1}{L_{fl}} & 0 & 0 & 0 & 0 & 0 & \frac{1}{L_{rr}} \end{pmatrix}^T. \quad (24.3.13)$$

with the control input given as the pressure inside the two chambers of the master brake cylinder

$$\mathbf{u} = \begin{pmatrix} p_{II} \\ p_I \end{pmatrix}. \quad (24.3.14)$$

The output of the model is chosen as the total displaced volume, thus it is the sum of the individually displaced volumes, calculated by the output distribution vector

$$\mathbf{c}^T = (1 \ 0 \ 1 \ 0 \ 1 \ 0 \ 1 \ 0) \quad (24.3.15)$$

and the direct feed-through vector

$$\mathbf{d}^T = (C_{II} \ C_I). \quad (24.3.16)$$

As was already mentioned, the pressure-flow characteristics of the hydraulic control unit are flow direction dependent due to the presence of backflow valves. Thus, the turbulent resistance is given as

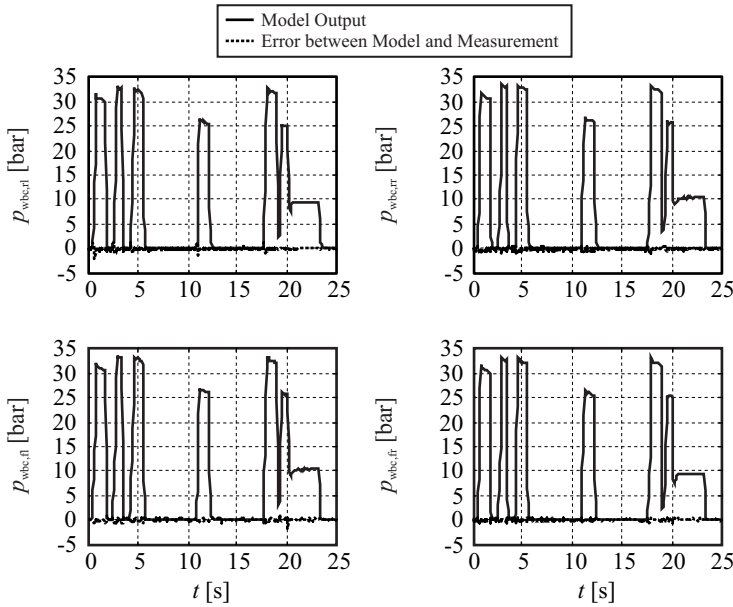


Fig. 24.56. Simulation run of the pressure buildup in the wheel brake cylinders

$$R_{T,i} = \begin{cases} R_{Ta,i} & \text{for } \dot{V}_i \geq 0 \\ R_{Tr,i} & \text{for } \dot{V}_i < 0 \end{cases} \quad \text{for } i \in \{\text{fl, fr, rl, rr}\}. \quad (24.3.17)$$

Now, the individual parameters of the model have been determined by iterative optimization based on measurements taken at the testbed in Fig. 24.55. The high fidelity of the derived model can be seen from the simulation in Fig. 24.56. Further details are described in (Straky et al, 2002; Straky, 2003).

Vacuum Brake Booster

The introduction of disc brakes required higher operation forces which in turn mandated some means to amplify the control forces exerted by the driver. Coming up with an easy yet efficient design, the vacuum brake booster is applied. Besides this amplification of the driver input, the vacuum brake booster is also used as an actuation device for the braking system by the brake assistant (Kiesewetter et al, 1997) which initiates a full braking in case of an emergency.

Figure 24.57 shows a cut-away drawing of the vacuum brake booster depicting the different parts of the vacuum brake booster. A photo is shown in Fig. 24.58. The foot-force exerted by the driver is supplied to the vacuum brake booster via the linkage. The vacuum brake booster is divided into two chambers by means of the diaphragm. The vacuum chamber is always kept at a pressure substantially lower than the atmospheric pressure, whereas the pressure in the working chamber is controlled

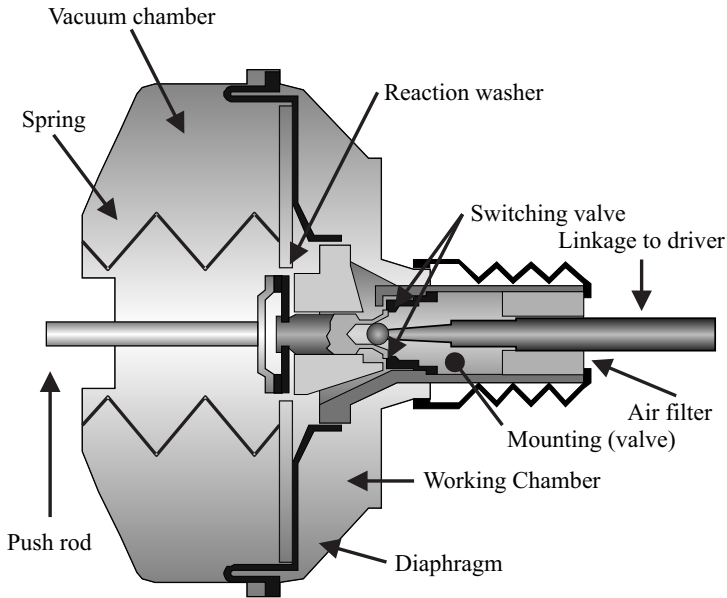


Fig. 24.57. Cut-away drawing of a vacuum brake booster



Fig. 24.58. Photo of a vacuum brake booster

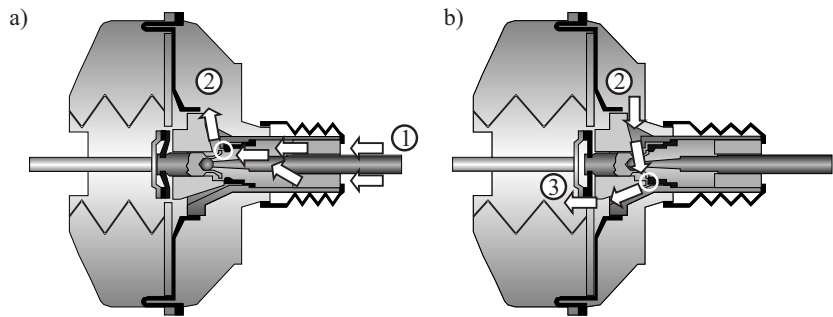


Fig. 24.59. Booster in (a) brake stage, (b) release stage

by the pneumatic valves located inside the vacuum brake booster. These valves allow to open or shut a flow path from the working chamber to the vacuum chamber (Fig. 24.59a) or from the working chamber to the surroundings (Fig. 24.59b) respectively. Opening and closing of the valves is controlled by the reaction washer, which is basically an elastic rubber disc. The air drawn from the surroundings is traversing an air filter and thereby cleaned. For spark ignition engines, the vacuum pressure is taken from the engine manifold, whereas for Diesel engines, the vacuum pressure is supplied by a vacuum pump. For operation at the testbed (Fig. 24.55), the vacuum brake booster is supplied with vacuum pressure by means of a membrane pump, thus this setup mimics a car equipped with a Diesel engine.

The pressure difference between the two chambers of the vacuum brake booster exerts a force onto the membrane, which is transmitted to the master brake cylinder via a push-rod. For a more detailed description of the vacuum brake booster, the reader is referred to (Robert Bosch GmbH, 2007; Burckhardt, 1991; Breuer and Bill, 2006).

In the following, the quantities are denoted as

p	pressure	V	volume
m	mass	R	gas constant
T	temperature	x	displacement
A	area	A_v	valve opening area
ϱ	density	v	velocity

and indices

vc	vacuum chamber	wc	working chamber
mem	membrane, i.e. diaphragm	amb	ambient
link	linkage		

will be used.

As was indicated in the previous section, the vacuum brake booster consists of two chambers. The chambers are modeled as pneumatic storage devices (Isermann, 2005). The state of such a storage device is described by the equation of state for an ideal gas,

$$p(t)V(t) = m(t)R_{\text{air}}T, \quad (24.3.18)$$

where p is the pressure, V the currently enclosed volume, m the mass of the enclosed air, R_{air} the gas constant and T the temperature. The mass m is chosen as the conservative quantity. The volume of the vacuum chamber (vc) is determined by the initial volume of the vacuum chamber, $V_{\text{vc},0}$, and the displacement of the diaphragm, x_{mem} ,

$$V_{\text{vc}} = V_{\text{vc},0} - x_{\text{mem}}A_{\text{mem}}. \quad (24.3.19)$$

The cross-sectional area of the membrane is written as A_{mem} . Volume and pressure changes are assumed to be isothermal. From the mass of the enclosed air, which was chosen as the conservative quantity, one can calculate the pressure inside the vacuum chamber as

$$p_{\text{vc}}(t) = \frac{m_{\text{vc}}R_{\text{air}}T}{V_{\text{vc}}} \quad (24.3.20)$$

and the actual density as

$$\rho_{\text{vc}} = \frac{m_{\text{vc}}}{V_{\text{vc}}}. \quad (24.3.21)$$

For the working chamber (wc), similar equations can be derived as

$$V_{\text{wc}} = V_{\text{wc},0} + x_{\text{mem}}A_{\text{mem}} \quad (24.3.22)$$

$$p_{\text{wc}} = \frac{m_{\text{wc}}R_{\text{air}}T}{V_{\text{wc}}} \quad (24.3.23)$$

$$\rho_{\text{wc}} = \frac{m_{\text{wc}}}{V_{\text{wc}}}. \quad (24.3.24)$$

Now, the valves are modeled. For this endeavor, Bernoulli's equation (Isermann, 2005) is employed. The fluid is assumed to be barotropic, since the behavior of air can be approximated by a barotropic fluid. In this case, Bernoulli's equation is given as

$$\int_1^2 \frac{\partial v}{\partial t} + \left(P_2 + \frac{v_2^2}{2} + U_2 \right) - \left(P_1 + \frac{v_1^2}{2} + U_1 \right) = 0 \quad (24.3.25)$$

The influence of the first term, which describes the acceleration induced pressure loss, is neglected. The terms P_i with $i \in \{1, 2\}$ describe the energy expenditure for the compression respectively expansion phases and are calculated as

$$P_I = \int_{p_0}^{p_1} \frac{dp}{\rho} = R_{\text{air}}T \int_{p_0}^{p_1} \frac{dp}{p} = R_{\text{air}}T \ln\left(\frac{p_1}{p_0}\right). \quad (24.3.26)$$

Bernoulli's equation is now applied to the flow path from point 1 to point 2, as shown in Fig. 24.59, which results in

$$R_{\text{air}}T \ln\left(\frac{p_1}{p_2}\right) + \frac{v_1^2}{2} - \frac{v_2^2}{2} = 0. \quad (24.3.27)$$

Point 1 is in the surroundings, therefore the velocity v_1 is assumed to be negligibly small, and the pressure p_1 is set to the atmospheric pressure p_{amb} . Point 2 is located

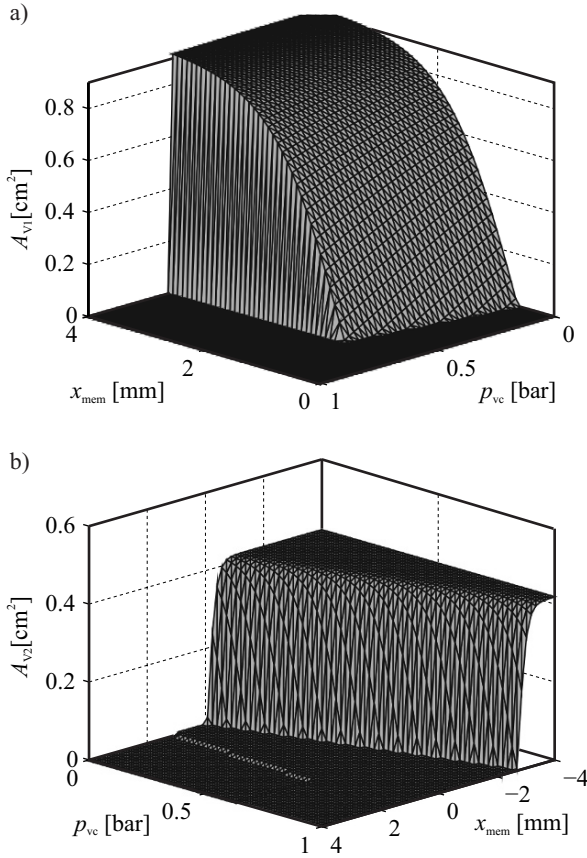


Fig. 24.60. Valve 1 opening function (a) and valve 2 opening function (b) of the vacuum brake booster

inside the working chamber, thus the pressure p_2 is identical to p_{wc} . One can now solve Eq. 24.3.27 with respect to v_2 as

$$v_2 = \sqrt{2R_{\text{air}}T \ln\left(\frac{p_{\text{amb}}}{p_{wc}}\right)}. \quad (24.3.28)$$

The mass flow into the working chamber is then determined as

$$\dot{m}_{wc} = A_{V1} \rho_{wc} v_2, \quad (24.3.29)$$

where A_{V1} is the active cross-sectional opening area of the aforementioned valve between the surroundings and the working chamber. Similarly, the equation governing the behavior of the valve between the working chamber and the vacuum chamber can now be derived. The flow path is shown in Fig. 24.59 and yields

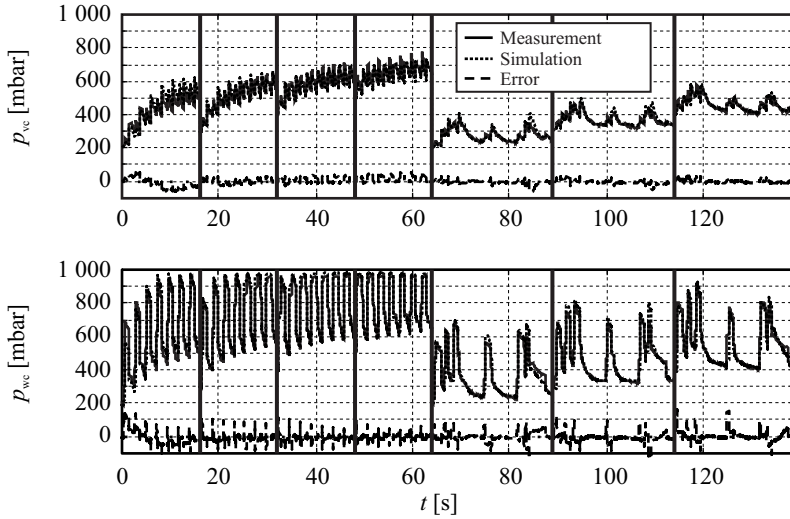


Fig. 24.61. Comparison of model and process output

$$v_3 = \sqrt{2R_{\text{air}}T \ln\left(\frac{p_{\text{wc}}}{p_{\text{vc}}}\right)} \quad (24.3.30)$$

$$\dot{m}_{\text{vc}} = -\dot{m}_{\text{wc}} = A_{\text{V2}}\rho_{\text{VC}}v_3. \quad (24.3.31)$$

The active cross-sectional areas of the two valves as a function of the membrane and pedal displacement and the active chamber pressures have been derived from experimental data gathered at the testbed. The resulting valve characteristics are shown in Fig. 24.60. For the identification, an iterative optimization approach was used employing the output error between the simulated and the real chamber pressures and using the Gauss-Newton algorithm with numerically determined derivatives. The model structure was a hybrid physical and black-box model. The pneumatics were modeled physically, whereas the valve opening functions were modeled as black-box functions. Further details are shown in (Muenchhof et al, 2003).

24.3.3 Automotive Suspension

Both, the suspension as well as the tire pressure, covered in the next section, have a large influence on the vehicle dynamics and are thus highly safety critical. In the following, identification techniques will be developed that allow to identify the characteristics of the vehicle suspension and the tire and can serve for supervision of these components.

For application either in a service station, for example for technical inspection, or in a driving state, it is important to use easily measurable variables. If the methods should be used for technical inspection, then the additional sensors must be easily mounted to the car. For on-board identification, the existing variables for suspension

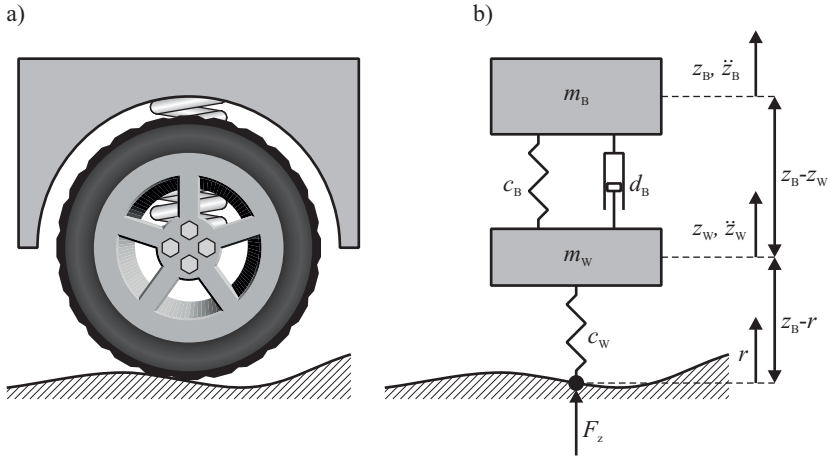


Fig. 24.62. Quarter car model. (a) Quarter car (b) schematic of the mechanical system

control should be used. Variables which meet these requirements are the vertical accelerations of body and wheel, \ddot{z}_B and \ddot{z}_W , and the suspension deflection $z_W - z_B$. Another important point is that the methods should require only little a priori knowledge about the type of car.

A scheme for a simplified model of a car suspension system, a quarter car model, is shown in Fig. 24.62. The following equations follow from force balances

$$m_B \ddot{z}_B(t) = c_B(z_W(t) - z_B(t)) + d_B(\dot{z}_W(t) - \dot{z}_B(t)) \quad (24.3.32)$$

$$m_W \ddot{z}_W(t) = -c_B(z_W(t) - z_B(t)) - d_B(\dot{z}_W(t) - \dot{z}_B(t)) + c_W(r(t) - z_W(t)) \quad (24.3.33)$$

In this section, the following symbols are used:

a_1, b_1	parameters of transfer functions	F_W	wheel force
c_B	stiffness of body spring	m_B	body mass
c_W	tire stiffness	p_W	wheel pressure
d_B	body damping coefficient	r	road displacement
f_r	resonance frequency	z_B	vert. body displacement
F_C	Coulomb friction force	z_W	vert. wheel displacement
F_D	damper force	$\Delta z_{WB} = z_B - z_W$	suspension deflection
F_S	spring and damper force		

The small damping of the wheel is usually negligible. A survey of passive and semi-active suspensions and their models is given in (Isermann, 2005).

In general, the relationship between force and velocity of a shock absorber is nonlinear. It is usually degressive and depends strongly on the direction of motion of the piston. In addition, the Coulomb friction of the damper should be taken into

account. To approximate this behavior, the characteristic damper curve can be divided into m sections as a function of the piston velocity. Considering m sections, the following equation can be obtained.

$$\ddot{z}_B = \frac{d_{B,i}}{m_B(\dot{z}_W - \dot{z}_B) + \frac{c_B}{m_B}(z_W - z_B) + \frac{1}{m_B}F_{C,i}}, \quad i = 1, \dots, m, \quad (24.3.34)$$

compare (24.3.32). $F_{C,i}$ denotes the force generated by Coulomb friction and $d_{B,i}$ the damping coefficient for each section. Using (24.3.34) the damping curve can be estimated with a standard parameter estimation algorithm measuring the body acceleration \ddot{z}_B and suspension deflection $z_W - z_B$. The velocity $\dot{z}_W - \dot{z}_B$ can be obtained by numerical differentiation. In addition, either the body mass m_B or the spring stiffness c_B can be estimated. One of both variables must be known a priori. Using (24.3.32) and (24.3.33), other equations for parameter estimation can be obtained, e.g. (24.3.35) which can be used to estimate the tire stiffness c_W additionally

$$z_W - z_B = -\frac{d_{B,i}}{m_B}(\dot{z}_W - \dot{z}_B) - \frac{c_B}{m_B}(z_W - z_B) + \frac{c_W}{c_B}(r - z_W) - \frac{1}{c_W}F_{C,i} \quad (24.3.35)$$

The disadvantage of this equation is the necessity to measure the distance between road and wheel ($r - z_W$), see also (Bußhardt, 1995; Weispfenning and Leonhardt, 1996) for modeling and identification of the automotive suspension.

To test the above method in a driving car, a medium class car, an Opel Omega, Fig. 24.63, was equipped with sensors to measure the vertical acceleration of body and wheel as well as the suspension deflections. To realize different damping coefficients, the car is equipped with adjustable shock absorbers at the rear axle, which can be varied in three steps. In Fig. 24.65, the course of the estimated damping coefficients at different damper settings is given for driving over boards of height 2 cm, see Fig. 24.64.

After approximately 2.5 s, the estimated values converge to their final values. The estimated damping coefficients differ approximately 10% from the directly measured ones. In Fig. 24.66, the estimated characteristic curves at the different damper settings are shown. The different settings are separable and the different damping characteristics in compression and rebound is clearly visible, although the effect is not as strong as in the directly measured characteristic curve. More results are given in (Börner et al, 2001).

Next, the damping characteristics of the shock absorber were adjusted during a driving maneuver. Recursive parameter estimation then allow to adapt the damping coefficient accordingly. Figure 24.67 illustrates the suspension deflection $z_W - z_B$, the first derivative of the suspension deflection calculated with a state variable filter $\dot{z}_W - \dot{z}_B$, and the wheel acceleration \ddot{z}_W for the right rear wheel during a highway test drive. After 30, 60, 90, and 120 s, a change of the shock absorber damping was made.

Several estimations have shown that the recursive least squares algorithm (RLS) with exponential forgetting factor received very good results. This recursive parameter estimation is able to adapt to the different damping settings in about 10 s, see Fig. 24.68.



Fig. 24.63. Car for driving experimental for model validation and parameter estimation



Fig. 24.64. Driving experiment with wooden plates to excite the vertical dynamics

Table 24.5. Specifications of the Opel Omega for driving experiments

Parameter	Value
Type	Opel Omega A 2.0i
Year	1993
Drive	Rear wheel drive
Top speed	190 km/h
Engine	4 cylinder OHC spark ignition engine
Engine displacement	$1.998 \times 10^{-3} \text{ m}^3$
Rated power	$85 \times 10^{-3} \text{ Nm/s}$ at 5 200 rpm
Max torque	170 Nm at 2 600 rpm
Max drag torque	−49 Nm
Max rpm	5 800 rpm
Transmission	5 speed manual transmission
Brakes	Disc brakes at all four wheels
Steering	Continuous ball race power steering
Steering transmission ratio	13.5
Tire size	195/65 R15 91H
Rim size	6 J × 15
Tire radius of unloaded wheel	0.320 m
Tire rotational inertia	0.9 kg m^2
Unsprung mass front wheel	44 kg
Unsprung mass rear wheel	46 kg
Length	4.738 m
Width	1.760 m
Wheel base	2.730 m
Height of cog	0.58 m

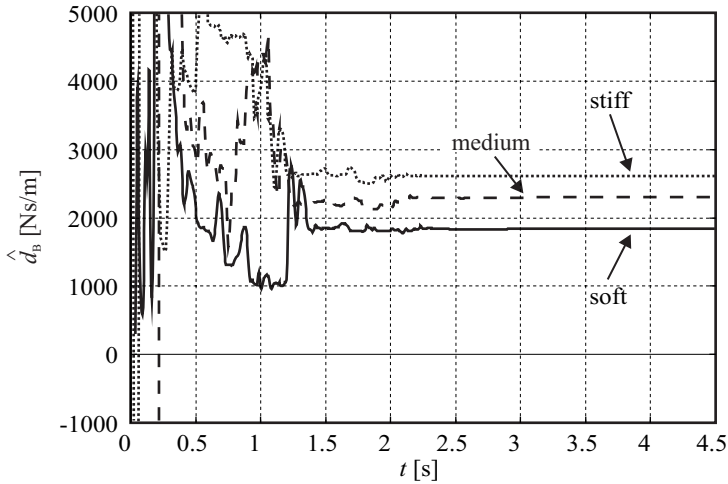


Fig. 24.65. Estimated damping coefficients for different damper settings (speed about 30 km/h)

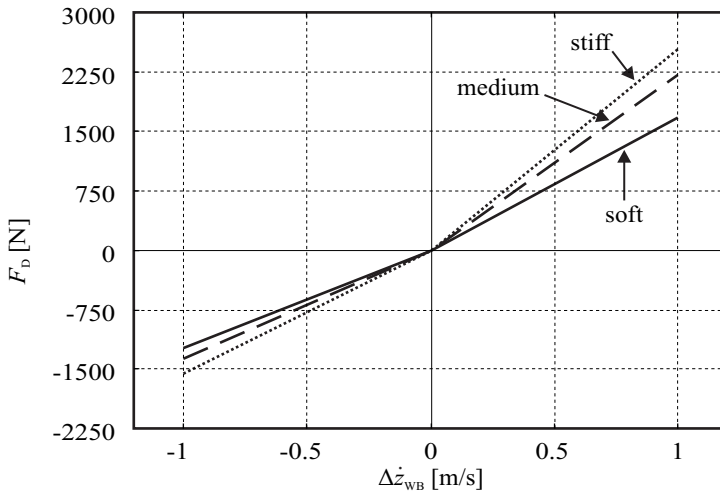


Fig. 24.66. Estimated characteristic damping characteristics for different damper settings

24.3.4 Tire Pressure

The tire pressure is also a very important quantity for vehicle safety. A survey conducted by Michelin in 2006 within the safety campaign “Think Before You Drive” has shown that only 6.5% of the 20 300 inspected cars had the required tire pressure at all four wheels. More than 39.5% of the cars had at least one extremely underinflated tire (< 1.5 bar) (Bridgestone, 2007). It is well known that it is dangerous to drive with underinflated tires. First of all, the risk of an accident increases due to the worse

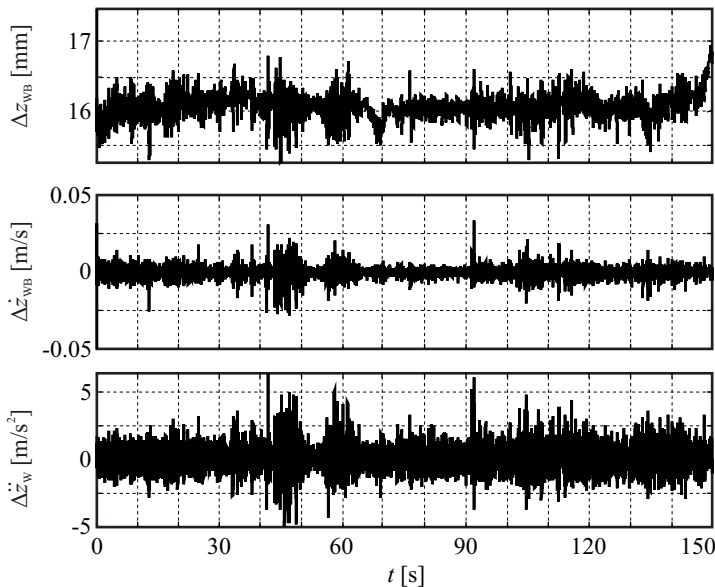


Fig. 24.67. Measured signals on a highway with variation of the damper configuration

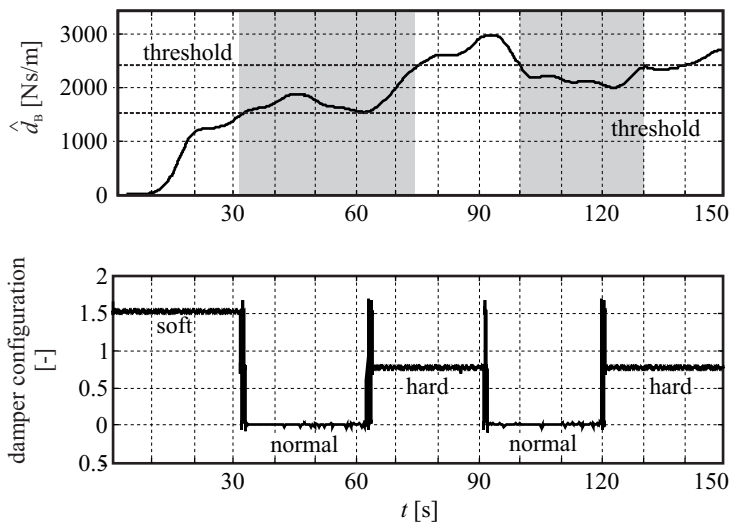


Fig. 24.68. Parameter estimate of the damping coefficient with RLS and forgetting factor. $0 < t < 3$ s: soft damping configuration, $30 \text{ s} < t < 60 \text{ s}$ and $90 \text{ s} < t < 120 \text{ s}$: medium damping configuration (normal situation), $60 \text{ s} < t < 90 \text{ s}$ and $120 \text{ s} < t < 150 \text{ s}$: hard damping coefficient

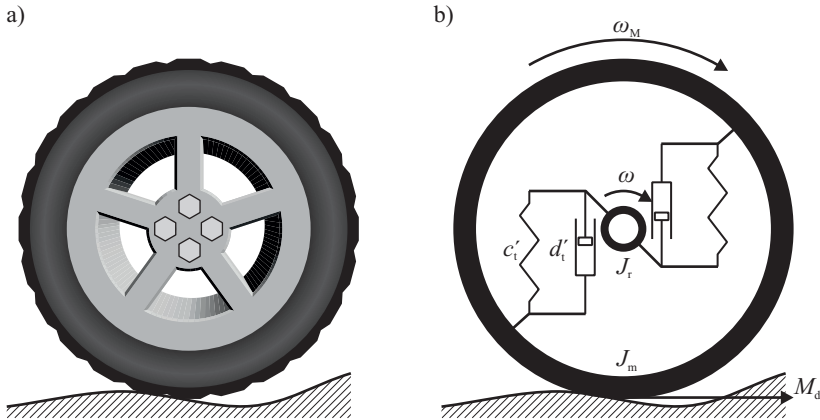


Fig. 24.69. Model of Torsional Wheel Oscillations

vehicle dynamic properties and the increased probability of a tire burst. Because of the increasing deformation, the tire heats up and its structure destabilizes (Normann, 2000). Furthermore, tire deflation increases fuel consumption and tire wear.

One can in general discern two approaches in tire pressure measurement systems. Direct measurement and indirect measurement. Direct tire pressure measurement systems use dedicated pressure sensors (Normann, 2000; Maté and Zittlau, 2006; Wagner, 2004). As the sensor is mounted directly at the tire, it is exposed to extreme environmental conditions, such as a wide temperature range and large accelerations. Also, the power supply of the sensor and the data transmission increase the cost and complexity of the systems. Therefore, one is interested in employing alternative measurement principles.

These are the basis of indirect tire pressure measurement systems. Here, one uses measured signals of the wheel or suspension that are already measured for the use by other vehicle dynamics control systems. One example is the wheel speed that is measured by the wheel speed sensors for use by the ABS system. Besides the wheel speed ω , also the vertical wheel acceleration \ddot{z}_w can be used to determine the tire pressure, as will be shown in the following.

Torsional Wheel Speed Oscillations

At the mantle of the wheel, a disturbing torque M_d attacks. This torque is caused by variations in the friction coefficient as well as variations of the height of the road surface. This and the elasto-kinematic bearings cause oscillations, which are transferred from the wheel speed at the mantle, ω_m to the wheel speed of the rim ω (Persson et al, 2002; Prokhorov, 2005).

Figure 24.69 shows a schematic diagram of the dynamics of these torsional wheel oscillations. The elasto-kinematics between the wheel and the rim are characterized

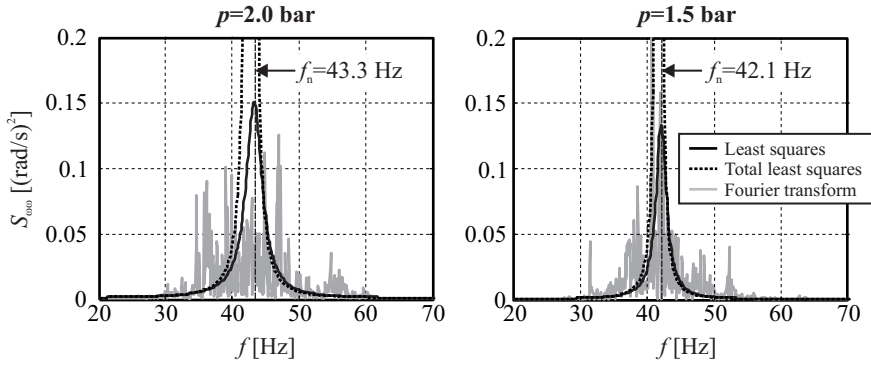


Fig. 24.70. Estimated power spectral density of the wheel speed signal for a straight driving maneuver with $v = 50$ km/h and a pressure of $p = 2.0$ bar and $p = 1.5$ bar respectively of the rear left tire

by a torsional stiffness c'_t and a torsional damping d'_t . The moments of inertia are denoted by J_m and J_r respectively. With these quantities, the transfer function from the disturbance torque M_d to the wheel speed ω is given as

$$G(s) = \frac{\omega(s)}{M_d(s)} = \frac{d'_t s + c'_t}{j_r J_m s^3 + (J_r + J_m) d'_t s^2 + (J_r + J_m) c'_t s} . \quad (24.3.36)$$

The torsional stiffness c'_t depends on the tire pressure. Changes in the tire pressure can be detected by analyzing the wheel speed signals. In order to detect changes in the tire pressure, one determines the spectrum of the wheel speed ω . This is done employing parametric spectral analysis methods.

The filter $G(z)$ was modeled as an auto-regressive process, i.e.

$$y(k) = q(k) - a_1 y(k-1) - a_2 y(k-2) - \dots - a_n y(k-n) . \quad (24.3.37)$$

The model parameters can then be determined e.g. by the method of least squares or the method of total least squares.

For the wheel speed analysis, the majority of all spectral components is concentrated in the low frequency range (< 10 Hz). Only small peaks exist in the frequency range above 10 Hz. As the spectral components that are influenced by the tire pressure are expected between 40 Hz and 50 Hz (Persson et al, 2002; Prokhorov, 2005), a bandpass filter is applied to attenuate spectral components outside of this frequency band. The experimental results of test drives with different tire pressure are shown in Fig. 24.70. One can see that the estimation of the power spectral density of the wheel speed signal by means of the Fourier transform has many peaks and is very disturbed. Hence, the resonance maximum is difficult to detect. Application of the parametric spectral analysis results in a much smoother spectrum. The power spectral density obtained by the spectral analysis with the method of least squares matches well with the general shape of the spectrum as estimated using the Fourier transform.

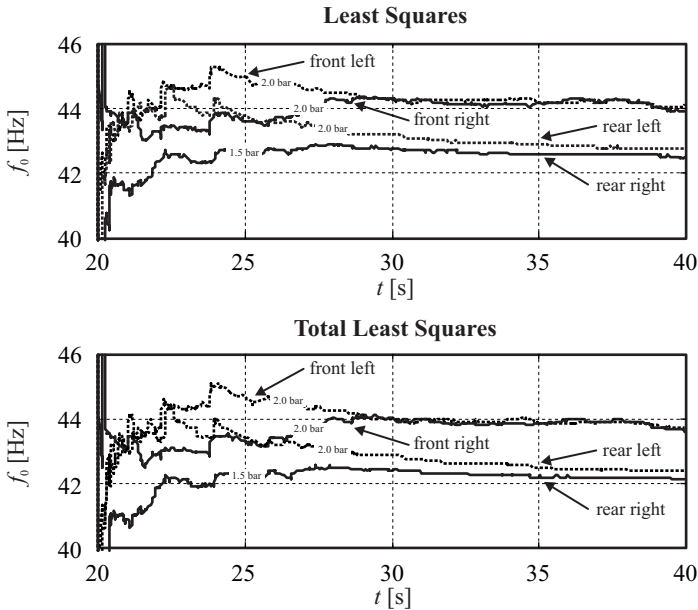


Fig. 24.71. Recursive estimation of the power spectral density of the wheel speed signal for a straight driving maneuver with $v = 50$ km/h. Rear right tire underinflated at $p = 1.5$ bar, all other tires correctly inflated at $p = 2.0$ bar. Power spectral density characterized by the natural frequency f_0

Although the maximum of the power spectral density obtained by using the method of total least squares is far too large, the resonance frequency is still identified well. By the method of least squares, the resonance of the correctly inflated tire is located at 43.3 Hz and for the deflated tire, reduces to 42.1 Hz.

To be able to detect changes in the tire pressure during operation of the vehicle, recursive parameter estimation methods will now be used to estimate the power spectral density of the wheel speed signal online. Instead of identifying the resonance frequency, the natural frequency f_0 will now be identified as it is less affected by wear of the suspension system (Isermann, 2002).

Figures 24.71 and 24.72 show experimental results. In Fig 24.71, the rear right tire was underinflated at $p = 1.5$ bar, whereas all other tires correctly inflated at $p = 2.0$ bar. One can see that the detection of changes in tire pressure is possible. Note that the rear axle is the driven axle of the car and equipped with a differential gear. Due to the coupling by differential gear, the rear left wheel is also affected although inflated properly.

Vertical Wheel Acceleration

Signals from the suspension system are also influenced by the tire pressure (Börner et al, 2002; Weispfenning and Isermann, 1995; Börner et al, 2000), such as e.g. the

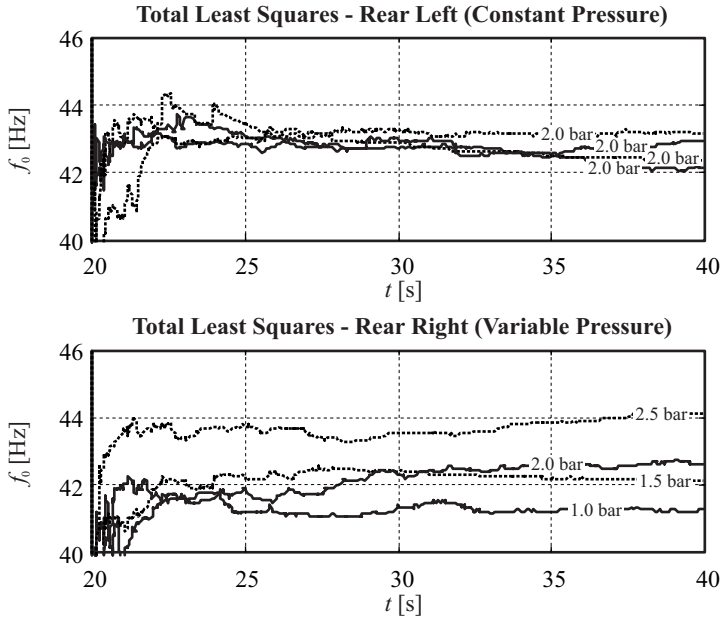


Fig. 24.72. Recursive estimation of the power spectral density of the torsional wheel oscillations for a straight driving maneuver with $v = 50$ km/h. Pressure in rear right tire varied from 1.0 bar up to 2.5 bar

spring deflection z_{wb} , the vertical body acceleration \ddot{z}_b , or the vertical wheel acceleration \ddot{z}_w . As the body motion z_b , \ddot{z}_{bb} is much slower than the wheel motion z_w , \ddot{z}_w , one cannot expect to see the effect of varying tire pressure in the body motion (Börner et al, 2000). Considering the quarter car model in Fig. 24.62, one can derive a transfer function from the road height r to the wheel acceleration \ddot{z}_w neglecting the movement of the body, i.e. $z_b = 0$, as

$$G(s) = \frac{\ddot{z}_w(s)}{z_h(s)} = \frac{\frac{c_w}{c_b + c_w} s^2}{\frac{m_w}{c_b + c_w} s^2 + \frac{d_b}{c_b + c_w} s + 1}. \quad (24.3.38)$$

Since the tire stiffness depends on the tire pressure, one can observe changes in the tire pressure in the spectrum of \ddot{z}_w .

Experimental results for this method are shown in Figs. 24.73 through 24.75. For the analysis of the vertical wheel acceleration spectrum, there are few neighboring frequency peaks from other effects and hence no filter is required. Figure 24.73 shows that resonance frequency can be clearly detected and the spectrum is strongly sensitive to changes in the tire pressure. The difference of f_0 between the correctly inflated tires and the underinflated tire is larger when the total least squares spectral analysis is used instead of the least squares spectral analysis. In Fig. 24.75, a strong dependence between the deflation of the left tire and the respective tires natural frequency f_0 is observable. Hence, the vertical wheel acceleration shows stronger

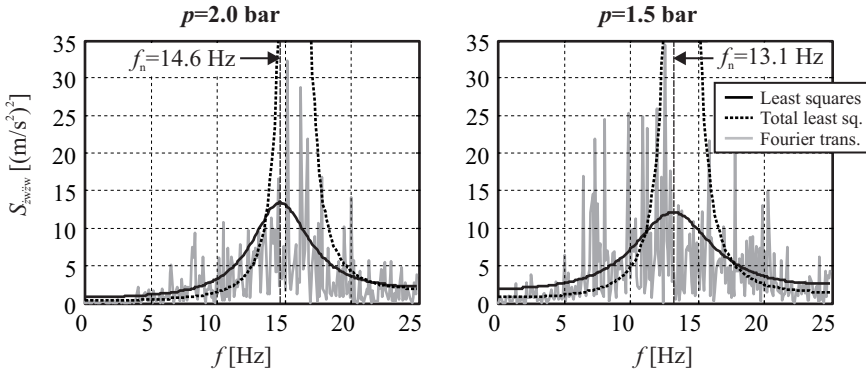


Fig. 24.73. Estimated power spectral density of the vertical wheel acceleration for a straight driving maneuver with $v = 50$ km/h and a pressure of $p = 2.0$ bar and $p = 1.5$ bar respectively of the rear left tire

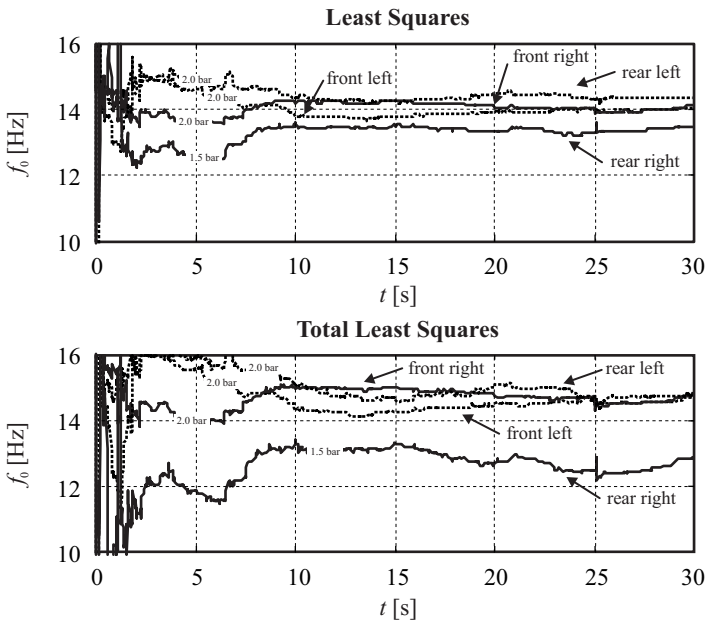


Fig. 24.74. Recursive estimation of the power spectral density of the vertical wheel acceleration for a straight driving maneuver with $v = 50$ km/h. Rear right tire underinflated at $p = 1.5$ bar, all other tires correctly inflated at $p = 2.0$ bar

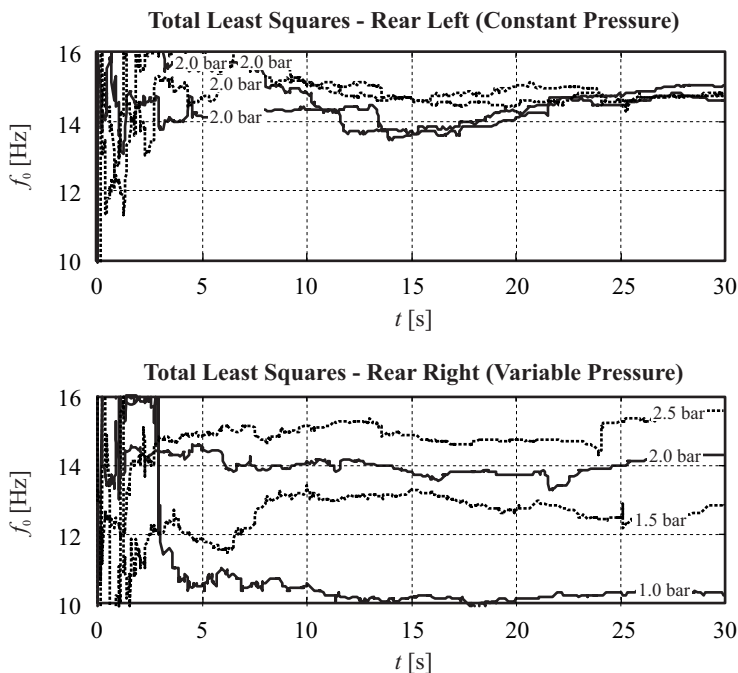


Fig. 24.75. Recursive estimation of the power spectral density of the vertical wheel acceleration for a straight driving maneuver with $v = 50$ km/h. Pressure in rear right tire varied from 1.0 bar up to 2.5 bar

dependence on the tire pressure than the torsional wheel oscillations. A survey on tire pressure monitoring with direct and indirect measurements is given in (Fischer, 2003).

24.3.5 Internal Combustion Engines

In the following, the identification of models of internal combustion engines for passenger cars shall be treated. The results can be applied to manifold areas of application for internal combustion engines. In contrast to earlier combustion engines as well as modern gasoline engines, Diesel engines require up to 8 manipulated variables and 8 control variables to meet the ambitious perspectives for low fuel consumption and emissions. Therefore, multi-variable non-linear control is necessary, where the underlying non-linear MIMO models are identified on testbenches. In the following, a Diesel engine is considered as an example of identification of combustion engine models.

Modern Diesel engines are equipped with the following mechatronic actuators:

- High pressure injection system with multiple injections
- Variable camshaft

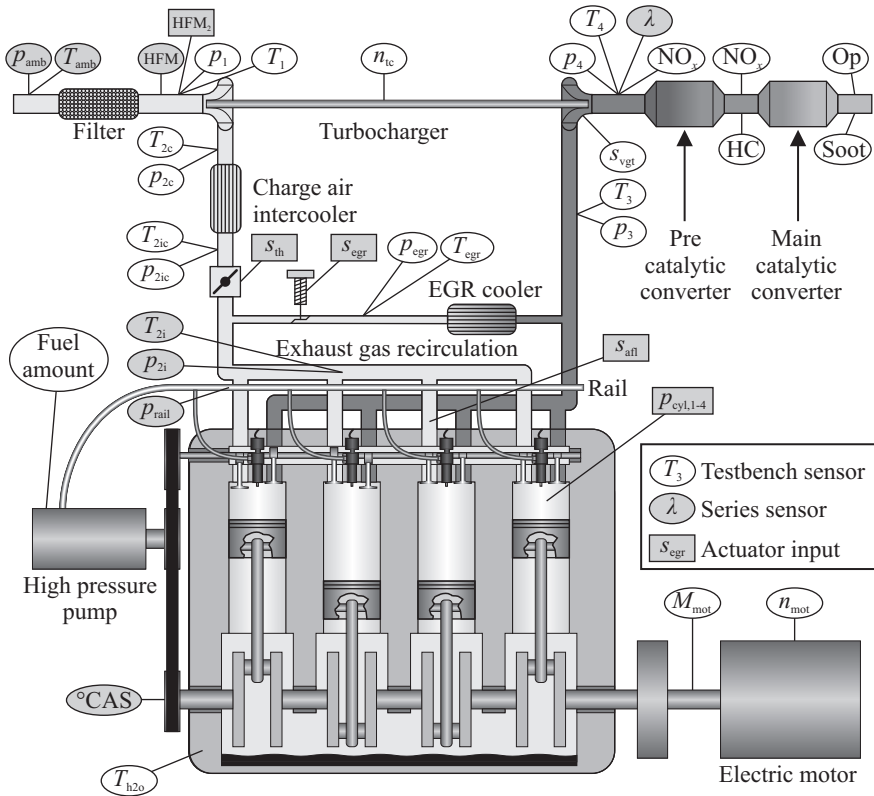


Fig. 24.76. Schematic view of a modern Diesel internal combustion engine with (HFM denotes hot film air mass flow sensor)

- Variable geometry turbo charger
- Exhaust gas recirculation

As was already stated above, these actuators lead to an increase in the number of controlled variables, which all influence the static and dynamic behavior. In a strive for reduced fuel consumption and reduced emissions, one is interested in precise static or also dynamic models of the Diesel engine, which then allow to optimize the engine controllers employed in the engine control unit. The derivation of dynamic engine models becomes more important as recent studies have shown that up to 50% of the emissions of a dynamic driving cycle are caused by accelerations, (Gschweidl and Martini, 2004). The key question in identification of engine models is how the measurement time can be reduced as the huge increase in the number of parameters to be varied has lead to an exponential increase in required measurement time. Here, special attention is paid to the design of the input sequence as to minimize the measurement time while still obtaining models of high fidelity, (Schreiber and Isermann, 2009). The symbols used in this section are:



Fig. 24.77. Control stand

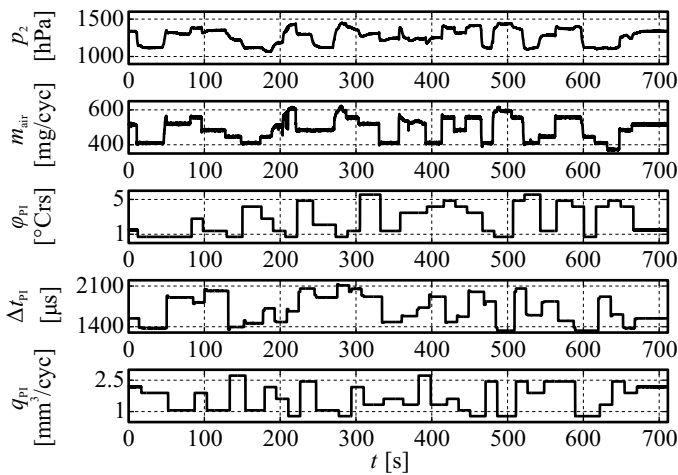


Fig. 24.78. Internal combustion engine on a testbench

m_{air}	air mass in combustion chamber
p_2	boost pressure
φ_{PI}	crank angle of pilot injection
Δt_{PI}	duration of pilot injection
q_{PI}	quantity of fuel of pilot injection
q_{MI}	quantity of fuel of main injection
NO_x	nitrogen-oxides

Table 24.6. Specifications of the vgt turbo-charged Diesel internal combustion engine, type Opel Z19DTH

Parameter	Value
Engine displacement	1.91
Engine power	110 kW
Number of cylinders	4
Torque	315 Nm at 2 000 rev
Bore \times stroke	82 mm \times 90.4 mm
Emission level	Euro 4

**Fig. 24.79.** Input signals for internal combustion engine excitation. APRBS test signals for five inputs (simultaneous excitation of the engine at the operating point, $n_{Mot} = 2000$ rpm and $q_{MI} = 20 \text{ mm}^3/\text{cyc}$ (Isermann and Schreiber, 2010))

In the following, some experimental results will be presented that have been obtained at an internal combustion engine testbed, see Fig. 24.77. These examples are taken from (Schreiber and Isermann, 2007) and (Isermann and Schreiber, 2010).

The internal combustion engine is mounted on a cart (Fig. 24.78) and can be connected to an asynchronous motor that allows to put a certain torque load on the engine to conduct measurements in different load regimes. The experiments have been conducted on an Opel Z19DTH Diesel engine, whose specifications can be found in Table 24.6.

Figure 24.79 shows a test signal sequence that has been used to conduct measurements at the process. As the behavior of the internal combustion engine is highly non-linear, an APRBS signal has been used for identification, where also the amplitude of the signal is varied in contrast to the two-valued binary PRBS signal. The input signal was furthermore designed to be D-optimal.

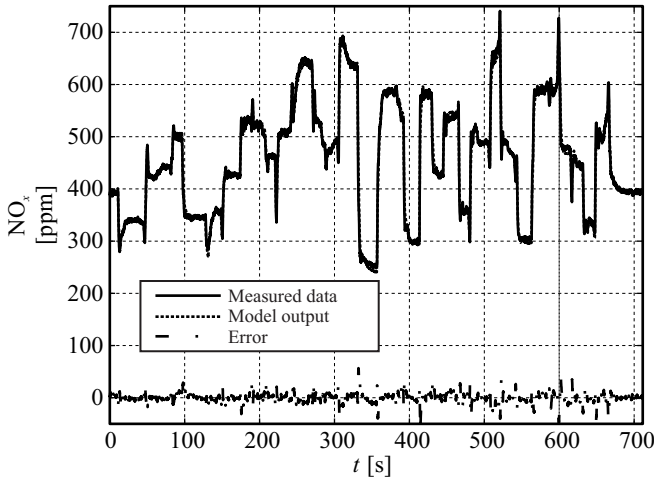


Fig. 24.80. Measured data and model output for NO_x model (Isermann and Schreiber, 2010)

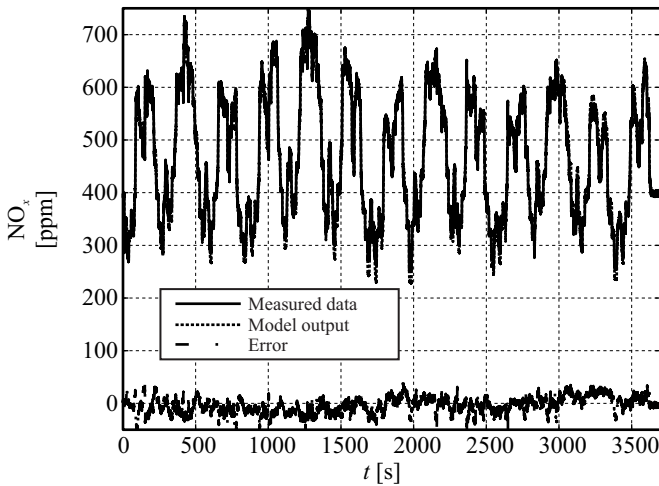


Fig. 24.81. Generalization results for NO_x model for $n_{\text{Mot}} = 2000 \text{ rpm}$ and $q_{\text{MI}} = 20 \text{ mm}^3/\text{cyc}$ (Isermann and Schreiber, 2010)

As an example of a non-linear dynamic MISO model, a model of NO_x emissions has been derived using the LOLIMOT neural network. The output of the neural net and the measurements used for the training are shown in Fig. 24.80. Generalization results are then presented in Fig. 24.81.

The identification of dynamic models has several advantages. First of all, in contrast to stationary measurements, one does not have to wait until the system has settled. Secondly, one can easily deduce a static model from the dynamic model by just

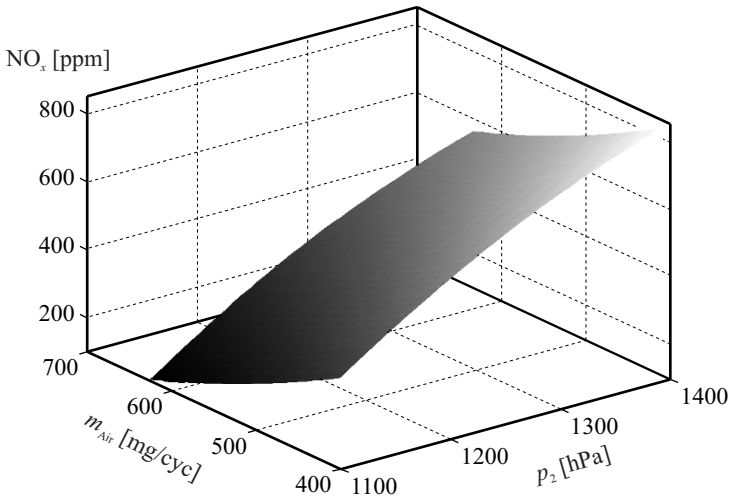


Fig. 24.82. Calculated stationary map for NO_x model for $n_{\text{Mot}} = 2000$ rpm and $q_{\text{MI}} = 20 \text{ mm}^3/\text{cyc}$ depending on air mass and boost pressure (Isermann and Schreiber, 2010)

calculating the static gain and neglecting the dynamics. The resulting stationary characteristics have been displayed in Fig. 24.82. With the same approach, other models of important dynamics have been identified as well. For the highly non-linear characteristics, the local linear net models are especially well suited for identification. A model of an internal combustion engine had also been the subject of Examples 20.1 and 20.3.

24.4 Summary

This chapter illustrated the use of identification techniques applied to different processes. As one can see from the wide area of applications that has been covered in this chapter, identification methods are a quite universal tools for the extraction of physical parameters and dynamics of processes and haven proven well in many applications. The successful application of identification methods necessitates a certain knowledge of the underlying process dynamics as well as the choice of the appropriate identification method.

For many applications, it is possible to provide physics-based equations that govern the static and dynamic behavior of the system. Then, the method of least squares has been applied for the parameterization based on input/output data. If one cannot provide (simple) equations for the dominant physical effects, one can use (selected) neural nets for identification and modeling. This has been shown for a combustion engine model and the heat exchanger with the LOLIMOT approach.

Other aspects that have been illustrated by the choice of examples are continuous-time and discrete-time models, non-linear models, time domain and frequency domain identification among others, see also Table 24.1. Further application examples can be found in the books (Isermann, 1992, 2005, 2006, 2010).

References

- Ballé P (1998) Fuzzy-model-based parity equations for fault isolation. *Control Eng Pract* 7(2):261–270
- Börner M, Straky H, Weispfenning T, Isermann R (2000) Model-based fault detection of vehicle suspension and hydraulic brake systems. In: *Proceedings of the 1st IFAC Conference on Mechatronic Systems*, Darmstadt
- Börner M, Zele M, Isermann R (2001) Comparison of different fault-detection algorithms for active body control components: automotive suspension system. In: *Proceedings of the 2001 ACC*, Washington, DC
- Börner M, Weispfenning T, Isermann R (2002) Überwachung und Diagnose von Radaufhängungen. In: Isermann R (ed) *Mechatronische Systeme für den Maschinenbau*, Wiley-VCH-Verlag, Weinheim
- Breuer B, Bill KH (2006) *Bremsenhandbuch: Grundlagen, Komponenten, Systeme, Fahrdynamik*, 3rd edn. ATZ/MTZ-Fachbuch, Vieweg, Wiesbaden
- Bridgestone (2007) Umweltbelastung durch Reifen mit zu wenig Druck. URL www.bridgestone.de
- Burckhardt M (1991) *Fahrwerktechnik: Bremsdynamik und PKW-Bremsanlagen*. Vogel Buchverlag, Würzburg
- Bußhardt J (1995) Selbsteinstellende Feder-Dämpfer-Last-Systeme für Kraftfahrzeuge: *Fortschr.-Ber. VDI Reihe 12 Nr. 240*. VDI Verlag, Düsseldorf
- Fischer M (2003) Tire pressure monitoring (BT 243). *Verlag moderne industrie*, Landsberg
- Freyermuth B (1991) Knowledge-based incipient fault diagnosis of industrial robots. In: *Prepr. IFAC Symposium on Fault Detection, Supervision and Safety for Technical Processes (SAFEPROCESS)*, Pergamon Press, Baden-Baden, Germany, vol 2, pp 31–37
- Freyermuth B (1993) Wissensbasierte Fehlerdiagnose am Beispiel eines Industrieroboters: *Fortschr.-Ber. VDI Reihe 8 Nr. 315*. VDI Verlag, Düsseldorf
- Geiger G (1985) Technische Fehlerdiagnose mittels Parameterschätzung und Fehlerklassifikation am Beispiel einer elektrisch angetriebene Kreiselpumpe: *Fortschr.-Ber. VDI Reihe 8 Nr. 91*. VDI Verlag, Düsseldorf
- Gschweidl K, Martini E (2004) Transient experimental design for the estimation of dynamic engine behavior. In: *Haus der Technik (ed) Motorenentwicklung auf dynamischen Prüfständen*, Wiesbaden, Germany
- Halbe I (2008) Modellgestützte Sensorinformationsplattform für die Quer- und Längsdynamik von Kraftfahrzeugen: *Anwendungen zur Fehlerdiagnose und Fehlertoleranz: Fortschr.-Ber. VDI Reihe 12 Nr. 680*. VDI Verlag, Düsseldorf

- Hensel H (1987) Methoden des rechnergestützten Entwurfs und Echtzeiteinsatzes zeitdiskreter Mehrgrößenregelungen und ihre Realisierung in einem CAD-System. Fortschr.-Ber. VDI Reihe 20 Nr. 4. VDI Verlag, Düsseldorf
- Isermann R (1987) Digitale Regelsysteme Band 1 und 2. Springer, Heidelberg
- Isermann R (1992) Identifikation dynamischer Systeme: Besondere Methoden, Anwendungen (Vol 2). Springer, Berlin
- Isermann R (2002) Lecture Regelungstechnik I. Shaker Verlag, Aachen
- Isermann R (2005) Mechatronic Systems: Fundamentals. Springer, London
- Isermann R (2006) Fault-diagnosis systems: An introduction from fault detection to fault tolerance. Springer, Berlin
- Isermann R (2010) Fault diagnosis of technical processes. Springer, Berlin
- Isermann R, Freyermuth B (1991) Process fault diagnosis based on process model knowledge. J Dyn Syst Meas Contr 113(4):620–626 & 627–633
- Isermann R, Schreiber A (2010) Identification of the nonlinear, multivariable behavior of mechatronic combustion engines. In: 5th IFAC Symposium on Mechatronic Systems, Cambridge, MA, USA
- Isermann R, Lachmann KH, Matko D (1992) Adaptive control systems. Prentice Hall international series in systems and control engineering, Prentice Hall, New York, NY
- Kiesewetter W, Klinkner W, Reichelt W, Steiner M (1997) Der neue Brake-Assistent von Mercedes Benz. atz p 330 ff.
- Mann W (1980) Identifikation und digitale Regelung eines Trommeltrockners: Dissertation. TU Darmstadt, Darmstadt
- Maté JL, Zittlau D (2006) Elektronik für mehr Sicherheit – Assistenz- und Sicherheitssysteme zur Unfallvermeidung. atz pp 578–585
- Milliken WF, Milliken DR (1997) Race Car Vehicle Dynamics. SAE International, Warrendale, PA
- Moseler O (2001) Mikrocontrollerbasierte Fehlererkennung für mechatronische Komponenten am Beispiel eines elektromechanischen Stellantriebs. Fortschr.-Ber. VDI Reihe 8 Nr. 908. VDI Verlag, Düsseldorf
- Moseler O, Heller T, Isermann R (1999) Model-based fault detection for an actuator driven by a brushless DC motor. In: Proceedings of the 14th IFAC World Congress, Beijing, China
- Muenchhof M (2006) Model-based fault detection for a hydraulic servo axis: Fortschr.-Ber. VDI Reihe 8 Nr. 1105. VDI Verlag, Düsseldorf
- Muenchhof M, Straky H, Isermann R (2003) Model-based supervision of a vacuum brake booster. In: Proceedings of the 2003 SAFEPROCESS, Washington, DC
- Normann N (2000) Reifendruck-Kontrollsystem für alle Fahrzeugklassen. atz (11):950–956
- Persson N, Gustafsson F, Drevo M (2002) Indirect tire pressure monitoring system using sensor fusion. In: Proceedings of the Society of Automotive Engineers World Congress, Detroit
- Pfeiffer K (1997) Fahrsimulation eines Kraftfahrzeuges mit einem dynamischen Motorenprüfstand: Fortschr.-Ber. VDI Reihe 12 Nr. 336. VDI-Verlag, Düsseldorf

- Pfeufer T (1997) Application of model-based fault detection and diagnosis to the quality assurance of an automotive actuator. *Control Eng Pract* 5(5):703–708
- Pfeufer T (1999) Modellgestützte Fehlererkennung und Diagnose am Beispiel eines Fahrzeugaktors. *Fortschr.-Ber. VDI Reihe 8 Nr. 749*. VDI Verlag, Düsseldorf
- Pfleiderer C, Petermann H (2005) Strömungsmaschinen, 7th edn. Springer, Berlin
- Prokhorov D (2005) Virtual sensors and their automotive applications. In: *Proceedings of the 2005 International Conference on Intelligent Sensors, Sensor Networks and Information Processing*, Melbourne
- Robert Bosch GmbH (2007) Automotive handbook, 7th edn. Bosch, Plochingen
- Schorn M (2007) Quer- und Längsregelung eines Personenkraftwagens für ein Fahrerassistenzsystem zur Unfallvermeidung. *Fortschr.-Ber. VDI Reihe 12 Nr. 651*. VDI Verlag, Düsseldorf
- Schreiber A, Isermann R (2007) Dynamic measurement and modeling of high dimensional combustion processes with dynamic test beds. In: *2. Internationales Symposium für Entwicklungsmethodik*, Wiesbaden, Germany
- Schreiber A, Isermann R (2009) Methods for stationary and dynamic measurement and modeling of combustion engines. In: *Proceedings of the 3rd International Symposium on Development Methodology*, Wiesbaden, Germany
- Straky H (2003) Modellgestützter Funktionsentwurf für KFZ-Stellglieder: *Fortschr.-Ber. VDI Reihe 12 Nr. 546*. VDI Verlag, Düsseldorf
- Straky H, Muenchhof M, Isermann R (2002) A model based supervision system for the hydraulics of passenger car braking systems. In: *Proceedings of the 15th IFAC World Congress*, Barcelona, Spain
- Vogt M (1998) Weiterentwicklung von Verfahren zur Online-Parameterschätzung und Untersuchung von Methoden zur Erzeugung zeitlicher Ableitungen. Diplomarbeit. Institut für Regelungstechnik, TU Darmstadt, Darmstadt
- Voigt KU (1991) Regelung und Steuerung eines dynamischen Motorenprüfstands. In: *Proceedings of the 36. Internationales wissenschaftliches Kolloquium*, Ilmenau
- W Goedecke (1987) Fehlererkennung an einem thermischen Prozess mit Methoden der Parameterschätzung: *Fortschritt-Berichte VDI Reihe 8, Nr. 130*. VDI Verlag, Düsseldorf
- Wagner D (2004) Tire-IQ System – Ein Reifendruckkontrollsystem. *atz* (660–666)
- Wanke P (1993) Modellgestützte Fehlerfrüherkennung am Hauptantrieb von Bearbeitungszentren. *Fortschr.-Ber. VDI Reihe 2 Nr. 291*. VDI Verlag, Düsseldorf
- Wanke P, Isermann R (1992) Modellgestützte Fehlerfrüherkennung am Hauptantrieb eines spanabhebenden Bearbeitungszentrum. *at* 40(9):349–356
- Weispfenning T, Isermann R (1995) Fehlererkennung an semi-aktiven und konventionellen Radaufhängungen. In: *Tagung “Aktive Fahrwerkstechnik”*, Essen
- Weispfenning T, Leonhardt S (1996) Model-based identification of a vehicle suspension using parameter estimation and neural networks. In: *Proceedings of the 13th IFAC World Congress*, San Francisco, CA, USA
- Wesemeier D, Isermann R (2007) Identification of vehicle parameters using static driving maneuvers. In: *Proceedings of the 5th IFAC Symposium on Advances in Automotive Control*, Aptos, CA